2012

Design and optimization of 2.5 dimension porous media micromodel for nanosensor flow experiments

Saade Alexis Bou-Mikael
Louisiana State University and Agricultural and Mechanical College, sboumi1@lsu.edu

Design And Optimization of 2.5 Dimension Porous Media Micromodel for Nanosensor Flow Experiments

A Thesis
Submitted to the Graduate Faculty of the
Louisiana State University and
Agricultural and Mechanical College
In partial fulfillment of the
requirements for the degree of
Masters of Science in Chemical Engineering

in

The Gordon A. and Mary Cain Department of Chemical Engineering

by

Saade Alexis Bou-Mikael
B.S., Louisiana State University, 2009
May 2012

Dedicated to my parents,

whose endless encouragement and support helped me through this journey.

Acknowledgements

I would first like to thank my advisors, Dr. Karsten Thompson and Dr. Dimitris Nikitopoulos for their guidance with the project, and for their excitement and encouragement throughout the past two years. I would also like to thank Dr. Clinton Willson for his suggestions and insight along the way and for joining my defense committee. I would like to thank the AEC for funding my research.

I thank Daniel Park for his work in generating the micromodels and the advice he's given me along the way during the design process. I thank Jason Guy for his work in micromilling the brass mold inserts. I want to thank Nathan Lane for providing me the FEM codes for which a huge portion of our work is based upon, and would like to thank my other labmates Pradeep Bhattad, Amin Mirsaeidi, Qiang Sheng, Tejas Narayana, Yijie Chen, and Tim Thibodeaux for their advice throughout this process.

I want to thank everyone in the Cain Department of Chemical Engineering for all of the help they have provided me throughout my (elongated) stay in this Department. You have provided me with the tools to move on into the next stage of my life with confidence and excitement.

Last but not least I would like to thank my family, Sami and Marta Bou-Mikael my parents, and Khalil and Youssef, my brothers, for supporting me through this opportunity here at LSU.

TABLE OF CONTENTS

DEDICATION……. ii

ACKNOWLEDGEMENTS……. iii

ABSTRACT…… vi

CHAPTER 1 INTRODUCTION……. 1

CHAPTER 2 BACKGROUND……... 4

2.1 Micromodels for Porous Media Research……. 4

2.1.1 Micromodel Fabrication Techniques…….. 4

2.1.2 Micromodel Designs……... 6

2.2 X-Ray Microtomography……... 9

2.3 Characterization Techniques…….. 10

2.3.1 Network Modeling Morphology and Network Generation……. 10

2.3.2 Statistical Techniques…….. 12

2.3.3 Flow Simulations……. 17

CHAPTER 3 DESIGN AND OPTIMIZATION TECHNIQUES…… 19

3.1 Overview……. 19

3.2 Design of the 2.5-Dimension Micromodel……. 20

3.3 Characterization Methods…….. 26

3.3.1 Network Morphology…….. 26

3.3.2 Capillary Pressure Curves from Quasi-Static Drainage Simulations…….. 28

3.3.3 Two-Point Correlation Function…….. 29

3.3.4 Chord Length Distribution Function…… 31

3.3.5 Minkowski Functionals…… 32

3.3.6 FEM Simulation……... 34

3.3.7 Permeability……. 36

CHAPTER 4 RESULTS AND DISCUSSION…….. 37
4.1 Network Morphology Results…….. 38
4.1.1 Overview and Results Table…….. 38
4.1.2 Pore Coordination Number…… 39
4.1.3 Inscribed Pore Diameter……. 41
4.1.4 Hydraulic Conductance…….. 42
4.2 Statistical Correlation Results……... 43
4.2.1 Two-Point Correlation Function Distribution…… 43
4.2.2 Chord Length Distribution……. 46
4.3 Capillary Pressure Curve (CPC) Results…….. 54
4.4 Permeability Results……. 56
4.5 Velocity Distribution Results……... 57
4.6 Comparison of the 2.5-D micromodels to 2-D micromodels…… 60
4.7 Design of the Low Resolution Micromodel…….. 62
CHAPTER 5 SUMMARY ……. 65
5.1 Conclusions……... 65
5.2 Future Works……. 68
REFERENCES…… 73
VITA…… 77

ABSTRACT

Micromodels are used to visualize and study pore-scale phenomena such as immiscible displacements in porous media, foam flow behavior, and CO_2 flooding. The understanding gained from these experiments can be used to develop models to predict future behavior of the reservoir. Most micromodels are constructed using lithography techniques that are restricted to 2D patterns that require artificial generation or manipulation of images to develop connected micromodels. Characteristics innate to the original rock structure are often lost or skewed in developing micromodels that bear little resemblance to the original media.

Alternative microfabrication techniques using a micromilling tool have allowed us to vary the floor height in a micromodel, thus giving some variation in the third dimension. We refer to these structures (with varying floor height and fixed ceiling, and which cannot have passages on top of one another) as 2.5D micromodels. Using a technique called depth averaging, in which we take a section of a 3D voxel image of porous media and project the solid voxels down while simultaneously pushing the void space above, we generate micromodels that may allow for more accurate representations of the pore structure in 3D rock.

The design of the etched pattern requires the selection of a specific depth (or number of XMCT image slice) over which to average the image data. The 2.5-D pattern was obtained by optimizing a series of parameters to ensure the structure and flow patterns matched as closely as possible to the equivalent 3D structure and flow as can be accommodated given the restricted dimensionality. Parameters considered include flow-based parameters, common statistical correlations, and a host of topological parameters obtained by network model generation techniques.

For a Boise sandstone core sample imaged at 5.07 μm/pixel, an optimized depth of 115 μm gave the most accurate measures across the range of parameters. However, due to constraints regarding the resolution of the micromilling process, a second series of flow simulations were conducted in the originally optimized region of interest (100-150 μm) for a lower resolution image that resulted in the selection of 130 μm to depth average. This design was then used to fabricate a brass mold insert. The process of developing the microchips for nanosensor experiments is currently in the stage of assembling the PMMA chips.

CHAPTER 1 INTRODUCTION

The emergence of nanotechnology and its unique characteristics that allow for stronger, lighter, and more controllable materials have the potential to radically and positively alter the oil and gas exploration and production industry. From the development of more highly controllable drilling fluids to the development of more powerful and durable sensory equipment, nanotechnology has near limitless opportunity to improve oil recovery. One of the potential applications for nanotechnology in upstream operations is in exploration. With the increasing demand for more sophisticated and detailed field characterization techniques, the ability to design and fabricate nanosensors that can be injected into a reservoir to improve recovery of hydrocarbon resources is of high priority to the industry (Pourafshary & et.al., 2009). Prior to use in the reservoir, nanotechnology is being researched in laboratory conditions to ensure that the expected behavior upon injection is well understood.

Micromodels have long been used to understand pore-scale physics in the geosciences. Although they are idealized structures, they have helped reveal many important phenomena including immiscible displacements in porous media, the flow behavior of foam, and the effects of varying CO_2 flooding factors on the displacement process and oil recovery mechanism. As visualization techniques improve and computer simulations continue to increase in scale, micromodel experiments continue to be important to understanding pore-scale phenomena, and can be used as a basis of comparison to improve the accuracy of new flow models.

In establishing quantitative relationships between the observed flow behavior of nanosensors and relevant characteristics of the rock, experimental visualization of the nanosensors behavior will allow us to gain insight on how nanosensors will act in the reservoir. Therefore, the development

of micromodels with realistic geometries is of high importance to the overall objective of developing a realistic model of nanoparticle flow through porous media.

Most micromodels are constructed using traditional etching or lithography techniques, and are therefore restricted to 2D patterns (although the actual channels are three dimensional of course). This presents two problems. First, immiscible fluids cannot flow in separate, connected pathways in two dimensions (except in parallel flow channels). Hence, they are not ideal for studying many important multiphase flow processes. Second, the etched patterns cannot be extracted directly from most consolidated rocks because 2D slices of low-porosity samples usually do not have connected porosity.

Alternative microfabrication techniques allow us to vary the floor height in a micromodel, thus giving some variation in the third dimension. We refer to these structures (with varying floor height and fixed ceiling, and which cannot have passages on top of one another) as 2.5D micromodels. They do not help address the first issue given above. However, they do allow patterns to be developed that have three-dimensional laminar flow patterns and which may allow us to more accurately represent the pore structure in a 3D rock.

In this work, we describe the design of a 2.5-D micromodel pattern derived from a 3D microCT image of a consolidated rock. The 2.5D pattern is obtained by optimizing a series of parameters to ensure that the structure and/or flow patterns in the micromodel match as closely as possible to the equivalent 3D structure and flow as can be accommodated given the restricted dimensionality. Parameters considered include flow-based parameters such as velocity distributions, permeability, capillary pressure curves, as well as a host of topological parameters obtained by network model generation techniques. Well-established statistical techniques for

characterizing porous media such as the two-point correlation function and chord-length distribution function were also used to compare the 2.5D models to the original 3D structures. Additional work has been completed to modify the optimum micromodel structure so that it could be fabricated at the resolution for which the micromilling equipment was capable. A brass mold has been etched with this design.

In the remainder of this work, we describe the optimization procedure and present a 2.5D pattern. Chapter 2 gives a background on previous micromodel fabrication techniques as well as porous media characterization methods. Chapter 3 elaborates on the design procedure regarding 2.5-D patterns and describes the characterization process and algorithms used in the optimization of the micromodel. Chapter 4 explains the results obtained on a Boise sandstone core sample obtained from an Advanced Energy Consortium member and provides a detailed discussion regarding the importance of specific parameters to the design process as well as the difficulty in translating certain topological features from the original 3D images to the 2.5D model. A comparison between the 2.5D pattern and a 2D pattern developed from the same region of the core sample is conducted, followed by a discussion of the final modifications required prior to submitting the design for fabrication. The final chapter, Chapter 5, provides a brief summary, conclusions, and an outline of the future works that will be conducted based on this research.

CHAPTER 2 BACKGROUND

2.1 Micromodels for Porous Media Research

Micromodels are useful tools to visualize microfluidics phenomena in porous media, and have provided valuable insight into pore-scale behavior not obtainable through core flood experiments. Two-dimensional micromodels designed to artificially replicate porous media have been used to study a variety of enhanced oil recovery methods, including dynamic immiscible displacement mechanisms (Chatzis & Dullien, 1983), surfactant flooding (Paterson, Hornof, & Neale, 1984), foam flow behavior (Owete & Brigham, 1987); (Armitage & Dawe, 1989), the effects of pressure on CO_2 foam displacement (Chang, Martin, & Grigg, 1994), near-miscible gas and SWAG injection (Sohrabi, Danesh, & Jamiolahmady, 2007), as well as CO_2 flooding (Sayegh & Fisher, 2008). Micromodels have also been used to study phenomena such as formation fines and permeability impairment (Muecke, 1979), the effects of pore structure on displacement efficiency (Wardlaw, 1980), reservoir wettability (Morrow, 1990), and drainage and capillary fingering (Cottin & Bodiguel, 2010).

2.1.1 Micromodel Fabrication Techniques

Porous media micromodels have been fabricated using a variety of techniques and materials. Most micromodels in recent studies have been fabricated using some form of photo-etching techniques on a glass, silicon, or polymer-based material. The selection of the material used for a micromodel typically depends on the objectives of the study, as each displays benefits and disadvantages to its use as outlined by (Javadpour & Fischer, 2008).

Experiments that require using high temperature and/or high pressure are best suited for glass micromodels, which can also handle more reactive and less neutral fluids better than polymer

micromodels. They are relatively easier to clean and reuse than polymer-based micromodels. Examples of experiments in glass models under harsh conditions include that by (Chang, Martin, & Grigg, 1994) who studied the effects of high pressure (<1300 psi) on CO_2 foam displacement, a study by (Sayegh & Fisher, 2008) in which a CO2 flood and WAG injection at 10 MPa (1450 psi) and 50°C (122°F) was conducted to simulate reservoir conditions, and more recently by (Sohrabi, Danesh, & Jamiolahmady, 2007) in which a high-pressure glass micromodel was used to conduct near-miscible gas and SWAG experiments at critical pressures (~5100 psi) of methane/n-decane mixtures.

Polymer micromodels have certain advantages over glass micromodels. Using current photo-lithography techniques, polymer micromodel pore channels can be as small as 1 μm in size, whereas glass micromodels are limited to roughly 30 μm minimum pore diameter (Javadpour & Fischer, 2008). Additionally, polymer micromodels can be substantially cheaper to produce. As opposed to glass micromodel production, for which photolithography techniques must be repeated each time a micromodel is produced, most methods used to produce polymer micromodels require the fabrication of a master mold. These need only be etched once, saving both time and material costs for photomask generation and chemical etching. An added benefit from using a master mold is that it provides excellent reproducibility between micromodels. Creating a casting mold helps limit differences between models due to chemical etching, thus promoting experimental reproducibility. The combination of cheap and accurate fabrication allows for experimentation without the need to aggressively clean the micromodels for future experiments, making polymer-based micromodels ideal for studies in which complete removal of the solute is challenging. Examples include colloid (Auset & Keller, 2004), nanoparticle transport, and precipitates (Browning & Fogler, 1996).

As stated above, most micromodels today are generated using some form of photo-etching technique. McKellar and Wardlaw (1982) first outlined the method to produce glass micromodels and give a detailed description of the etching process. Essentially all glass micromodels are produced by direct etching of the glass by a controlled-hydrofluoric acid attack. Polymer-based micromodels are developed from a master mold containing the negative of the final pattern to be used in the micromodel. Hot-embossing is used to essentially stamp the pattern into a polydimethylsiloxane (PDMS) or polymethyl methacrylate (PMMA) polymer, which is softened at high temperatures. The mold can be fabricated in a variety of ways. The most common method uses similar photolithography methods as described above; this is explained in more detail by Javadpour (2008). A technique used by Tsakiroglou and Avraam (2002) employs an excimer laser LIGA technique to first etch the design on a PMMA chip followed by a microelectroforming process to produce a nickel and copper based mold insert from the etched PMMA chip. The mold insert is then used to generate subsequent PMMA micromodels through hot-embossing. A third method of mold insert fabrication, which has been used in this study, uses an ultra precision micromachining device capable of etching critically machinable materials including brass and hardened steel. Multilevel patterns can be developed relatively easier than in photolithography methods. Once the mold insert is created, a hot-embossing system can be used to generate polymer microchips.

2.1.2 Micromodel Designs

Two-dimensional porous media micromodels vary as much in design as they do in fabrication methods. Micromodel patterns can be designed with various degrees of structural resemblance to real porous media depending on the purpose of the study. Muecke (1979) studied formation fines and permeability impairment with a micromodel created by sandwiching a monolayer of glass

chips sintered between two glass plates. Hornof and Morrow (1998) used a micromodel with slightly sintered glass packing to study the effects of interfacial tension on displacement. Although these types of designs display a form of heterogeneity and induce interesting flow behavior, they do not necessarily display the same characteristics and topology of actual porous media.

The two types of micromodel designs include those formulated directly from images or to replicate the topological features of porous media (imaged-based designs), and those designed with distinct patterns such as a grid, repeating grid, artificially generated design, or geometric designs.

Geometric designs, such as those used by Sohrabi (2007), Cottin et.al (2010), Zhang (2011), Jamoloei and Kharrat (2010), Chang (1994), Willingham (2008) and Owete and Brigham (1987) are not intended to replicate the structure of actual rock but instead geometric patterns, and can be homogeneous or heterogeneous. Owete and Brigham (1987) studied foam flow mechanisms on a homogeneous model with a hexagonal array of vertically-oriented cylindrical cones to create a network of interconnected channels in between. Jamoloei and Kharrat (2010) used a homogeneous structure with offset asterisk-shaped solid structures to study surfactant flooding in both dilute oil-wet and water-wet structures. Willingham et. al. (2008) used an array of homogenous cylindrical patterns etched onto silicon wafers to evaluate the accuracy of a lattice-Boltzmann simulation to capture mixing and reactions at the pore scale. Recently, Zhang, et.al. (2011) studied liquid CO_2 displacement in a dual permeability pore lattice-shaped micromodel.

Heterogeneous lattice patterns are also used frequently. Flow variability is created by manipulating the width and/or depth of each different channel. Cottin et. al. (2010) used a

quadrilateral-network of intersecting channels of differing widths to study invasion mechanism by a non-wetting fluid for capillary numbers varying over five orders of magnitude. Tsakiroglou and Avraam (2002) used an excimer laser etching method to generate grids with variation of the depth (15-90 μm) and width (10-25 μm) in each channel. Crandall (2008) developed a novel micromodel fabrication method using stereolithography and used an AutoCAD-based algorithm to generate a micromodel with uniformly distributed throat widths between .35 to 1.0 mm and a throat height varying between .2 and .8 in seven distinct layers. We have used the Crandall pattern (Figure 1) to create 2.5D patterned micromodels for studying particle trapping (Park, 2011).

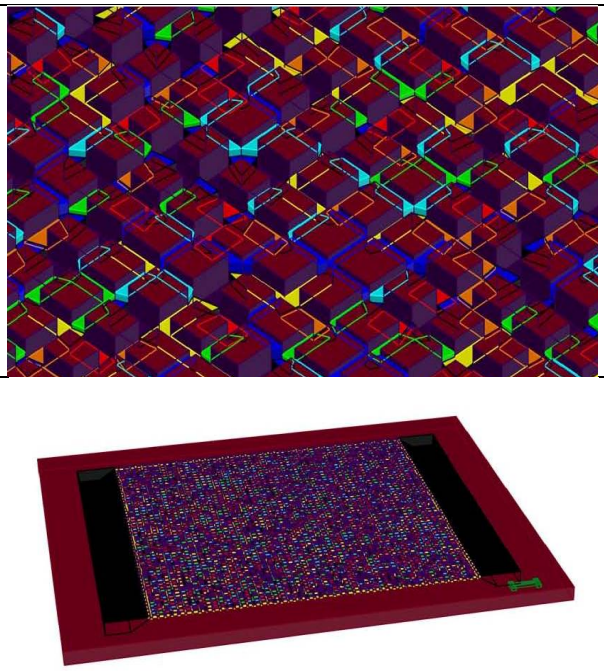

Figure 1. Porous Flow Device, Designed by Dustin Crandall (2008)

The second class of micromodel designs consists of image-based patterns. Hornbrook (1991) outlines a detailed method to generate two-dimensional micromodels from thin-slice images of rock. A high-resolution digitized image is obtained from microCT imaging of a core sample,

processed using image-segmentation to a binary (black and white) two-dimensional image of solid and pore space. A thresholding algorithm, typically dependent on a parameter such as porosity (Boek & Venturoli, 2010), is used to transform a 3-D image to a two-dimensional design to be fabricated. Image-based micromodels offer a more realistic pore geometry than geometric micromodels. Hornbrook (1991) used a thin slice of Berea sandstone and photolithography techniques to study the foam oil interactions. George et. al. (2005) constructed a silicon micromodel based on a representative sandstone sample to study the effect of viscosity on bubble coalescence. Boek (Boek, 2010) conducted micro-PIV experiments on a Berea-sandstone micromodel to validate the accuracy of his two-dimensional lattice-Boltzmann simulations. Mohiuddin (2011) performed studies of gravity-driven CO_2 displacement on a thin-section based glass micromodel. In a hybrid of geometric and image-based micromodels, Gunda, et.al. (2011) developed a micromodel by generating a 3-D pore network from the XMCT image and developing a 2-D pore network from a cross section.

2.2 X-Ray Microtomography

X-Ray Computed Microtomography (XMCT) is a noninvasive imaging technique in which x-rays are used to generate 2-D projections (slices) of a 3-dimensional object that when combined form a 3-dimensional reconstructed image of the object. Collimated x-ray beams from a synchrotron source are directed through a cross section of the object, where some of the incident beams are absorbed by the material as others pass directly through it. Contrast arises from the difference in the absorption by components of the material (van Dalen, 2003). The rays that pass through the sample are collected by a scintillator, which absorbs the x-ray energy and emits

energy in the form of light. A digital camera with a given spatial resolution can detect the light, and a single 2-D projection of the 3-D object is collected. The object is then rotated at small angles about an axis perpendicular to the x-ray beam to obtain a set of 2-D projections for the slice. An algorithm is used to construct the 2-D image of the core sample from the projections (McDowell, 2007), and the slices are stacked to generate the 3-D image of the object.

For our reconstructions, imaging was performed at the Center for Advanced Microstructures and Devices (CAMD) at Louisiana State University. The beamline for microtomography at CAMD transmits x-ray energy at 40 keV; the camera lens used to capture the scintillator light gives a spatial resolution at 5 microns/pixel.

2.3 Characterization Techniques

2.3.1 Network Modeling Morphology and Network Generation

Pore network modeling is numerical technique for modeling flow and transport in porous media, and involves replacing the continuum pore-space geometry in a real material with a simplified network of discrete pores and pore throats. Transport behavior is then modeled by solving the relevant conservation equations within the network. The process of discretizing the pore space from a microCT image has been well studied (Øren, Bakke, & Arntzen, 1998) (Sok & Knackstedt, 2002) and much emphasis has been made in the network modeling community to replicate the pore-structure as accurately as possible. Work by Bryant, et. al. (1993) spawned this work by introducing physically representative network models. These were distinct from previous network models because of their one-to-one direct mapping to a real 3D structure, which in turn enabled the network structures to retain specific spatial correlations unique to the

original porous media. Modern networks no longer use geometric characteristics as adjustable parameters which helps them be used in a predictive capacity.

Al-Raoush, Thompson and Willson (2003) present an overview of network generation techniques, including the medial-axis approach, the Delaunay-tessellation approach, and their modified Delaunay-tessellation method. There paper gives a detailed comparison of the established methods for unconsolidated porous media and can be reviewed for better understanding. The medial-axis approach uses the skeleton of the void space in porous medium and a morphological thinning algorithm to map the network pores and throats. Lindquist and Venkatarangan (1999) expanded on the medial-axis based network generation to develop algorithms to calculate characteristics of the network such as the pore body radius, pore throat radius, coordination number and other statistical data on the structure's geometry. Two significant problems occur using the original Delaunay-tessellation method that are addressed by the modified Delaunay-tessellation method. First, the use of tetrahedrons to map the pore structure generated pores all with fixed coordination numbers of four. Second, the method has a tendency to incorrectly identify pore locations and size by breaking single large pores into multiple tetrahedrons (pores). These problems are addressed with MDT while maintain the powerful computational efficiency of the original process. Essentially, an additional algorithm that uses inscribed spheres contained within the void space to determine if multiple pores generated by Delaunay-tessellation can be consolidated into one large pore. This allows for variable coordination numbers and provides better one-to-one correspondence between the original image and the network model.

These and similar methods can be used to create pore networks, which in turn can be used to characterize the porous medium. Each pore and throat holds morphological information such as

pore location, pore volume, pore inscribed radius, throat length, and pore-throat aspect ratio that. This information can be used to characterize the pore space, and in the current work is used to compare the 3D to the 2.5D structures.

2.3.2 Statistical Techniques

Various statistical correlation functions such as the chord-length distribution function and the two-point correlation function have been used to characterize rock structure (Hilfer, 1991), predict and estimate the macroscopic properties such as fluid permeability (Berryman & Blair, 1986), thermal conductivity, diffusivity, and elasticity (Roberts & Knackstedt, 1996), and synthesize artificial replications of porous media (Ioannidis & Chatzis, 2000). These techniques can be applied directly to the voxelized 3D images of porous media.

N-Point Correlation Functions

The *n*-point correlation functions (*n*=1,2,3…), as calculated for a three-dimensional image of a two-phase material, are a measure of the probability of finding n points lying within the same phase. Defining a function $f(\mathbf{x})$=0 or 1, where zero indicates a solid phase voxel, one a void phase, and $\mathbf{x}$ the spatial coordinate of the voxel, the void-phase one-point correlation function can be described as the probability that a randomly selected voxel $\mathbf{x}$ is in the void phase. This is equivalent to the void volume fraction, or the porosity ϕ, of the system:

$$\hat{S}_1 = \langle f(\mathbf{x}) \rangle = \phi \quad (1)$$

where the brackets < > indicate a volume average over the entire system.

The two-point correlation function is the probability that two randomly selected points at a given magnitude are in the same phase. The probability that the first selected point, **x**, is in the void phase is simply the porosity of the material. The probability that the second point at a distance **r** away from the original point is also in the void phase is calculated.

$\hat{S}_2 = \langle f(\mathbf{x}) f(\mathbf{x}+\mathbf{r}) \rangle = \phi \langle f(\mathbf{x}+\mathbf{r}) \rangle$	(2)

Assumptions for these equations are that the porous medium is statistically homogeneous and therefore have translational invariance, and locally isotropic such that averages do not depend on orientation. The n-point correlation function has been used to develop formulas to predict macroscopic properties of the material. Berryman and Blair (1986) highlight the properties of the two-point correlation function, $S_2(r)I$, for random porous media. For an isotropic material,

$S_2(0) = \phi$	(3)
$\lim_{r \to \infty} S_2(r) = \phi^2$	(4)
$S_2'(0) = -s/4$	(5)

where ϕ is the porosity, r is the distance from selected center point, and s is the specific surface area (internal surface area per unit volume). Debye et al. (1957) details the theorem that obtains the third equation. Berryman and Blair (1986) used data obtained from the one- and two-point correlation functions as parameters to calculate the permeability of the digital image to good agreement with experiments for high-permeability sandstones.

Chord Length Distribution Function

Torquato and Lu (1993) provide a complete description of the chord length distribution function, its relationship to the *Lineal Path Function* $L(x)$, and its specific use in two-phase porous media. For binary images, a chord can be defined as the length between two interfaces along a specific line across the image. Specifically, the chord length distribution $p(x)$ is the probability of finding a chord of length $x + dx$ entirely within a single phase of a two-phase system. The shape of the chord length distribution can be used to describe the homogeneity of the image. A sharper peak on the histogram correlates to a more homogeneous material.

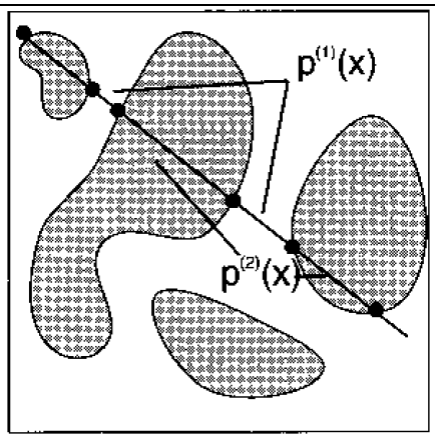

Figure 2. Graphical description of the chords formed by an arbitrary line. Image taken from the paper "Structure and transport properties of a porous magnetic gel via x-ray microtomography" by M.D. Rintoul, et.al., as published in Physical Review E, Sept. 1996.

Minkowski Functionals

An often used set of parameters to quantitatively characterize porous media are the Minkowski functionals, a set of four morphological measures obtained from integral geometry that describe the shape and connectivity of the image. For three-dimensional objects, the four functionals correspond to the enclosed volume, surface area, mean-breadth, and connectivity (by Euler Characteristic) of the system. A number of papers describe the fundamental mathematics of the

Minkowski functionals in great detail (Michielsen & De Raedt, 2000); (Mecke & Arns, 2005). The Minkowski functionals are invariant under rigid motions and additive, which lends them to be suitable for digital image analysis. Additivity indicates that for a functional M, the value of M for union of two disjoint sets M_A and M_B is simply the summation of M_A and M_B (Lehmann, 2008). The morphology of a two-phase complex image can be uniquely defined by the porosity φ, the surface area S, the integral mean curvature H, and the Euler characteristic, χ. For a three-dimensional digital image, the Minkowski functionals can be described by the following equations:

$M_0 = V$	(6)
$M_1 = \frac{S}{8}$	(7)
$M_2 = \frac{H}{2\pi^2}$	(8)
$M_3 = \frac{3}{4\pi}\chi$	(9)

Where V is the enclosed total volume, S is the surface area, H is the integral mean curvature, and χ is the Euler characteristic.

For a discretized 3D object, the four Minkowski functional can be obtained easily and are presented in an article by Michielsen and De Raedt (2002) as follows. Each individual cubic voxel can be described as the union of 8 vertices, 12 edges, 6 faces, and 1 cube interior. (Note that for the following equations, V, S, H, and χ are summations of voxel parameters)

$V = n_c$	(10)
$S = -6n_c + 2n_f$	(11)
$2H = 3n_c - 2n_f + n_e$	(12)
$\chi = -n_c + n_f - n_e + n_v$	(13)

Where n_c is the number cubes, n_f is the number of faces, and n_e is the number of edges, and n_v the number of vertices. For each of these summations, only the sum of the void phase voxels is considered, i.e. n_c is the summation of the total void voxels only, n_f only accounts for the void phase voxel's faces, etc. For 3-D voxel images, the maximum values for a single voxel are n_c = 1, n_f = 6, n_e = 12, and n_v = 8. Note that the Minkowski functionals are additive; therefore, for two nearest-neighbor voxels, the connecting faces, edges, and vertices are counted just once. For two next-nearest neighbor void voxels, the connecting edges and vertices are counted only once; etc. For example in Figure 3, n_c = 3 open cubes, n_f = 16 open faces, n_e = 27 open edges, and n_v = 16 open vertices.

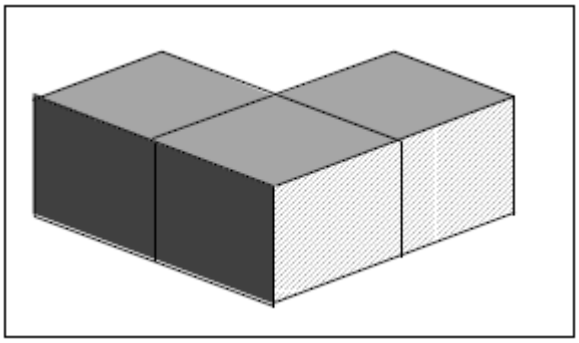

Figure 3. 3D object with three voxels. From Blasquez (2003).

2.3.3 Flow Simulations

Pore Network Modeling – Flow Simulations

In addition to a simplified representation of the pore space, pore network modeling uses a simplified mathematical model of fluid transport based on conservation equations. This allows for significant improvements in computational efficiency over other transport modeling techniques, and can therefore model significantly larger length scales than FEM or LBM, at the expense of streamline data.

For single-phase network modeling, the flow rate between pores can be calculated using the conservation equation:

$$q_{i,j} = \frac{g_{i,j}}{\mu}(P_j - P_i) \quad (14)$$

Since the diameters of the pore are significantly larger than the diameters of the throats connecting them, viscous forces are assumed to be negligible inside the pores. Pore throats act as resistors to fluid flow, with a hydraulic conductance term $g_{i,j}$ that is a function of the throat geometry providing flow resistance through viscous forces. A matrix of linear equations generated from mass conservation equations between pores are solved for the pressures at each pore. Once the pressure field is calculated across the network, permeability can be predicted using Darcy's equation. Network models have been used to model multiphase and reactive transport (Thompson & Fogler, 1997), solute & particle transport, and non-Newtonian flow (Balhoff & Thompson, 2006).

Finite Element Modeling

Traditional grid-based computational fluid dynamics (CFD) techniques use finite difference, finite volume, or finite element methods to solve the Navier-Stokes equations and continuity equation:

$\rho \frac{\partial \mathrm{u}}{\partial t} = \mu \nabla^2 \mathrm{u} - \rho(\mathrm{u} \cdot \nabla)\mathrm{u} - \nabla P + \rho g$	(15)
$\nabla \cdot \mathrm{u} = 0$	(16)

For low Reynolds number flow of a Newtonian fluid (common in porous media), the Navier-Stokes equation can be reduced to the linear Stoke's equation for creeping flow:

$\nabla P = \mu \nabla^2 \mathrm{u}$	(17)

This equation can be solved directly using any of the numerical methods mentioned above. Given a pore-scale 3D description of a porous medium, CFD simulations can be used to obtain local pressure and velocity throughout the pore space.

CHAPTER 3 DESIGN AND OPTIMIZATION TECHNIQUES

3.1 Overview

We present a novel design technique for a rock-based micromodel with varying floor depth, therefore inducing some three-dimensional flow behavior to the micromodel. As explained below, the pattern is designed through an optimization procedure in which flow and structure parameters in the micromodel are quantitatively measured against the same parameters in the three-dimensional rock.

While dependent on a number of factors, a typical single slice of rock imaged using microCT (e.g., the Berea Sandstone shown in Figure 4) cannot be used to generate a functional micromodel since there is no connectivity of the pore space (white) across the image. In three dimensions, most or all of this space becomes connected.

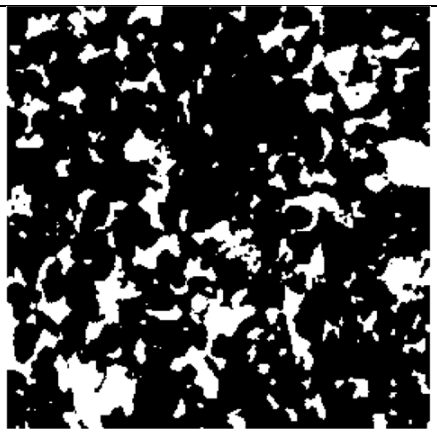

Figure 4. Single Slice of Berea Sandstone Imaged at 9 microns.

Depending on a number of factors, such as the rock topology, the image-segmentation process, and the resolution of the microtomography image, full connectivity of the pore space across the

micromodel requires a set of multiple adjacent slices. As shown in the pictures of varying levels of stacked images in Figure 5, for which black (white) regions indicates entirely solid (void) regions, the increase in the number of slices correlates with an increase in the connectivity of the pore space.

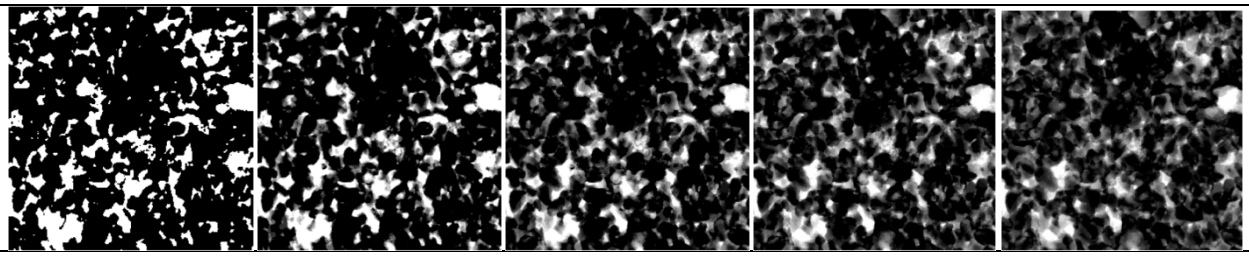

Figure 5. Horizontal view of Berea sandstone images, with increasing numbers stacked on top of each other. Black implies completely solid, white implies completely void space. From Left to Right 1 slice, 5 slices, 11 slices, 15 slices, and 21 slices averaged, respectively.

For 2-D micromodels, the creation of a micromodel requires some sort of manipulation of the image(s) to ensure connectivity. Hornbrook (1991) suggested the use of software packages and manual manipulation to ensure existence of a flow path across the image to be etched; that is, some form of thresholding over a number of layers in which areas of the micromodel are made void, followed by manual alteration of the void phase connections are required to ensure that fluid can flow across the micromodel.

3.2 Design of the 2.5-Dimension Micromodel

The two goals in designing the micromodels are (1) induce fluid movement in the vertical direction, or z-axis (which is not achievable with standard 2-D micromodels), and (2) to design a micromodel that replicates the structure and flow behavior of the actual material from which it is

generated. Preferably, this process would minimize manual processing of the structure or artificial generation of structures not obtained from the original image.

To attain these goals, we have devised a method to design and fabricate 2.5-D rock-based micromodels. These designs are obtained solely from the XMCT images of micromodel. The process consists of the following steps.

1.) Obtain a 3D cut out of the original rock, composed of multiple stacked 2-D images. (Figure 7-a)
2.) Select a yet-unknown subset of slices from the 3D data set to create a thin section of the image. (Figure 7-b)
3.) Within the thin section, project the solid voxels to the bottom (and inversely move the void voxels above), to create a depth-averaged void structure (Figure 6 and 7-c).
4.) Compare morphologic and dynamic flow parameters (2.5D micromodel versus 3D rock).
5.) Repeat steps 2-4 until an optimal number of slices has been determined.

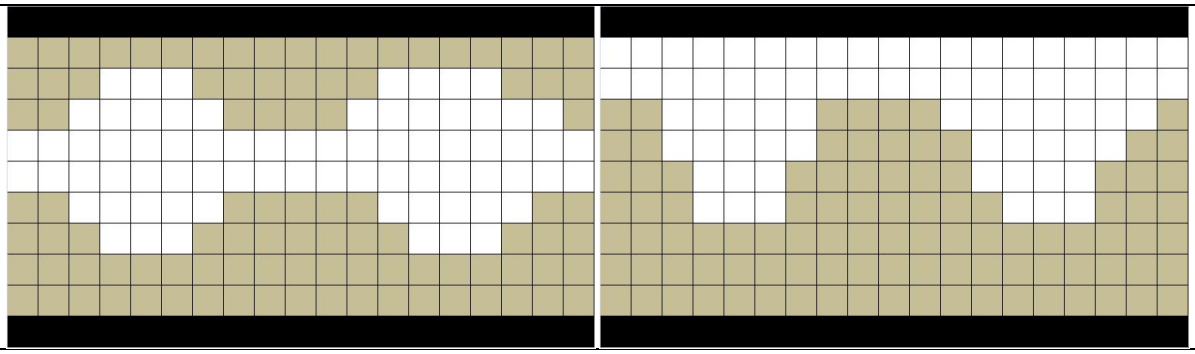

Figure 6. Side view of an example pore structure before depth averaging (left) and after depth averaging (right).

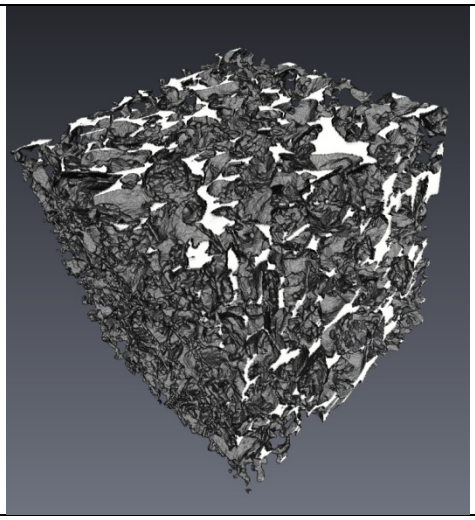

(a)

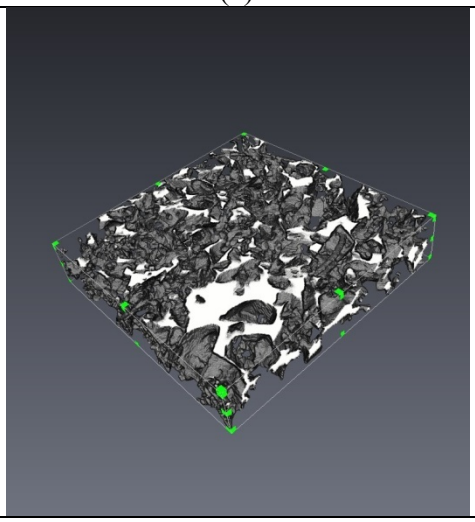

(b)

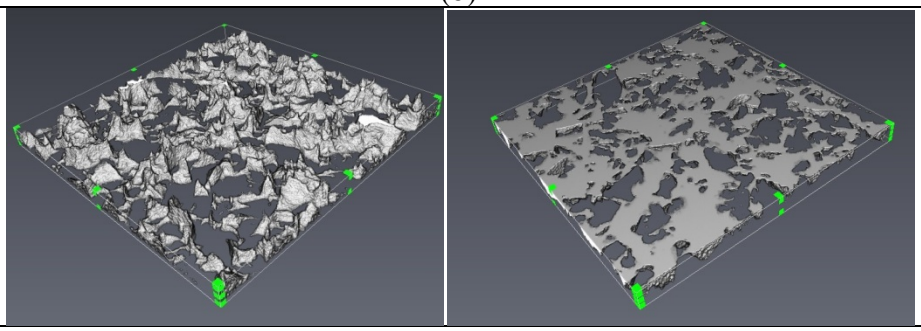

(c)

Figure 7. Visualization of the Depth averaging process. (a) The original segmented image prior to manipulation. (b) The sub-volume prior to depth averaging. (c) The depth averaged micromodel design from below (left) and above (right).

The transition from 3-D to the 2.5-D micromodel maintains a one-to-one mapping of the areal structure of the pore space. Hence, we expect to preserve much of the critical flow behavior (e.g., converging-diverging, and splitting and re-joining flows in Figure 8) in 2D, while at the same time inducing some moderate z-direction velocity.

A simple argument can be made to suggest that an optimum exists. Too few slices in the depth average will retain pore isolation and zero permeability across the micromodel. At the other extreme, too thick a region will combine overlapping pore regions over a majority of the micromodel, essentially rendering the structure to be similar to flow over a fractured surface. Clearly, somewhere between these two extremes is a range in which the pore space is connected yet retains typical pore and pore-throat geometries.

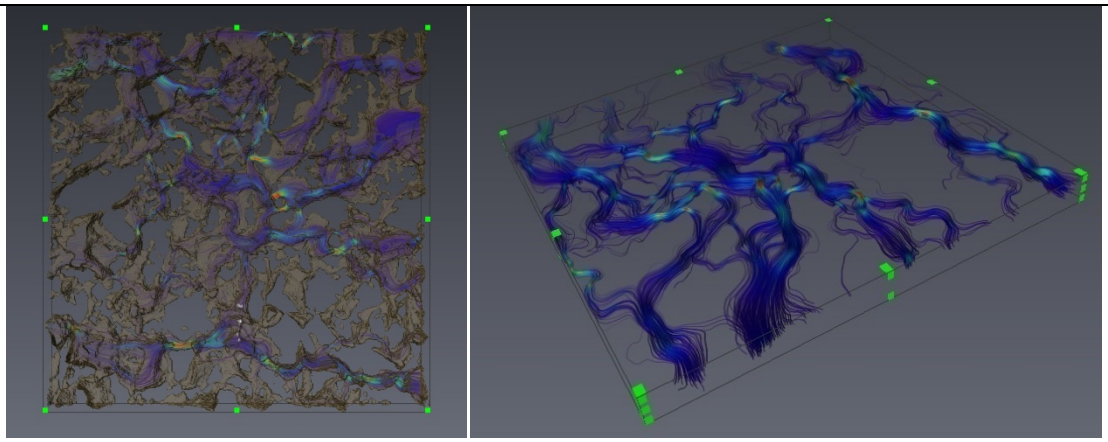

Figure 8. Aerial view (left) and perspective view (right) of a simulated flow field through a micromodel design.

Algorithm

Specific parameters can be obtained for each depth averaged micromodel design, compared to those of the original 3-D image of the rock sample, and tabulated to show an entire array of

characteristics to compare for the final depth selection. The characteristics to compare are left entirely to the micromodel designer, although we have selected parameters that aim to reproduce the flow behavior and topological characteristics of the original image. Our optimization process is outlined in a step-by-step approach.

1.) Parameters are generated for the original structure (process is identical to that of the depth averaged micromodels explained in the following steps).
2.) For the subset of depth averaged micromodel voxel images, the two point correlation function and chord length distribution functions are obtained directly from the voxel images of the designs and compared to the original structure.
3.) Networks are generated for each micromodel voxel image.
4.) Network morphological statistics are generated and stored in separate data files. A Matlab script scans the data files for maximum and minimum values for each parameter to use as boundary values for histogram generation. A sum of squares analysis is performed for each parameter.
5.) Capillary pressure curves are obtained using quasi-static drainage simulations on the networks. The step sizes for each test are dependent on the network and are thus different for each curve. A new set of data points interpolated at specific saturation values is obtained for each network. A sum of squares analysis is performed on the curves.
6.) The voxel images are brought from the High Performance Computing network server onto a local computer for mesh generation using AVIZO. Starting with the lowest depth average, a mesh made of connected tetrahedral elements is generated and uploaded back to the server in the Hypermesh format (Typical mesh size between .5 to 1.5 million elements).

7.) Simulations are performed and nodal values for the pressure and velocities are converted to voxel-base values. Permeability is also obtained from these simulations.

8.) In similar manner to Step 4, individual data sets for velocity profiles are processed using a simple Matlab algorithm for histogram generation and subsequent error analysis.

9.) Once all error analysis data is obtained and tabulated, selection of the optimum depth average is finalized.

Factors to Consider in Optimizing the Depth Average

The type of rock and its topological characteristics will affect the final depth average. Connectivity of the pore space may vary between consolidated rock and unconsolidated rock samples, between different types of consolidated rocks, i.e. sandstone, shale, and carbonate, and between different samples from the same formation. A structure with a lower porosity and more tortuous 3-D pore space may require a thicker depth to ensure connectivity across the final micromodel, while a high porosity, highly fibrous material may need a thinner slice to prevent originally disconnected, overlapping pore spaces being consolidated into the same micromodel pore space by the depth averaging process. One would also expect image resolution to play a role in selecting an optimum depth average.

Given the tortuous nature of porous media, pore space channels often lay directly above one another, which cause the combination of separate pores into larger pores as shown in Figure 9. As more layers are depth averaged, the frequency of this occurring increases.

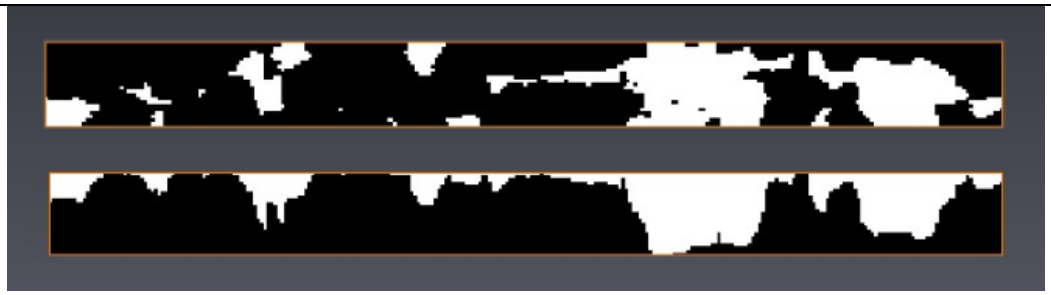

Figure 9. (a) Side view of a slice of rock cut out, before and after being depth averaged.

3.3 Characterization Methods

3.3.1 Network Morphology

The ability to characterize rock at the pore scale is of significant importance to modeling transport through porous media. Though methods such as the finite element method, lattice-Boltzmann, and particle-based approaches to modeling provide more detailed solutions than network models, a benefit of such extensive study of network modeling is the emphasis placed on network generation and replicating the pore-structure as accurately as possible. The information from these network-generating algorithms can be used to statistically characterize the porous medium. Histograms of parameters such as the pore coordination number, inscribed pore diameter, inscribed pore volume, throat-equivalent diameter, aspect ratio, throat conductivity, among others, can be obtained to give a comprehensive description of the image. Descriptions of the information obtainable from pore network generation are outlined below.

Pore and Throat Statistics

The **Pore Coordination Number** indicates the connectivity of a pore. For network models, it is defined as the number of throats connected to that pore. Determining pore coordination number from voxelized images is more challenging due to the dependence on voxel resolution, the range

of pore geometries found in natural porous media, and by network bonds not being aligned with Cartesian voxel geometry.

The **Inscribed Pore Diameter** is calculated using the maximum inscribed spheres associated with the pore, and is used to obtain the pore size distribution of the image. The pore size distribution is an important descriptor of a rock formation, indicating the level of heterogeneity within a system, and has a direct correlation to the capillary pressure curve for the system.

The **Inscribed Pore Volume** is a measure of the total volume for a given pore. For networks generated from voxel images, it is the sum of the volume of the voxels assigned to a specific pore.

In the algorithm, Throats have no volume and are defined from the faces where two pore elements come into contact. The **Inscribed Pore-Throat Diameter** indicates the maximum diameter of the cross-sectional area of the pore-throat interface. It is calculated as the diameter of the maximum inscribed sphere whose center lies on the surface separating two pores. This is also used in the equation to obtain the capillary pressure curves.

The **Pore-Throat Equivalent Diameter** is the diameter of the circle formed by creating a circle whose area is equal to that of the entire pore-throat interface.

The **Pore-Throat Aspect Ratio** is the ratio of the pore to pore-throat diameters, and is an important parameter for the study of two-phase flow and snap-off displacement.

The **Pore-Throat Length** is the measure of the distance between two connecting pores. It is an indicator of the connectivity of the system.

The **Throat-Hydraulic Conductivity** is used to calculate the permeability of the system, and can be calculated from a number of equations that are based on pore-throat geometry. It is a function of pore-throat radius, length, and pore-throat aspect ratio.

In characterizing the porous media sample and all subsequent micromodel designs based on the example, histograms were generated for each parameter of the original core sample as well as for each micromodel design. Histograms for the micromodel designs were then compared to the original core sample using a sum of squares error comparison to the Boise sandstone.

3.3.2 Capillary Pressure Curves from Quasi-Static Drainage Simulations

Capillary pressure is the most basic rock-fluid characteristic in multi-phase flow, and is an indication of the smaller pore being entered at a given saturation. (Lake, 1989). It is a function of the pore size distribution and is frequently used as a parameter in reservoir modeling. For our experiments, a quasi-static displacement was simulated on the network models developed from the micromodel designs. A quasi-static displacement simulation is capillary-pressure-dominated invasion of the non-wetting phase. Only equilibrium behavior is captured, and snap-off behavior is neglected in our simulations.

Starting at a pore space completely saturated with wetting phase fluid (S_w = 1), immiscible displacement was simulated until the final saturation measured 5% (S_w=.05), or until no further displacement occurred due to lack of pore space connectivity. For comparison between the micromodels and the original image, a sum of squares error is used to obtain an error between each micromodel CPC and the original CPC.

3.3.3 Two-Point Correlation Function

The two-point correlation function is an important statistical property of porous media that has been used to correlate the permeability, resistivity, and other physical properties to the porous media structure. The assumptions are that the porous medium of interest is statistically homogenous, and locally isotropic. Given the nature of the 2.5-D process and it's manipulation of the pore space, this is not accurate.

The manipulation by depth averaging rearranges the void voxels to be joined together above the solid voxels for a given column of voxels. For a high resolution XMCT image, depth averaging a few slices will add voxels of the same original pore. On the contrary, depth averaging at substantially large depths will begin to connect porous regions that are separate but overlapping, thereby increasing the overall size and connectivity of the void space. This will result in a micromodel that better resembles flow over a fractured surface than flow through porous media as shown in Figure 10.

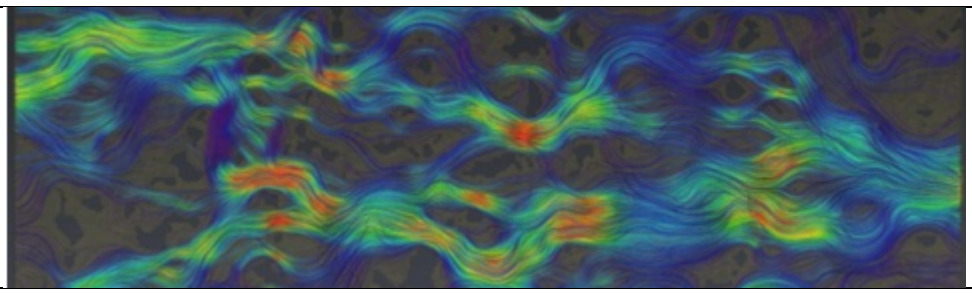

Figure 10. Image from a FEM simulation conducted for a micromodel based on a Berea sandstone imaged at 9 μm/voxel. This micromodel was depth averaged over 50 voxels, or 450 μm.

The local isotropy assumption becomes invalid since the probability that lower layers in the z-direction are solid will increase, while the probability of finding void on the top layer increases. As mentioned earlier, for an isotropic porous material,

$S_2(0) = \phi$	(3)
$\lim_{r\to\infty} S_2(r) = \phi^2$	(4)
$S_2'(0) = -s/4$	(5)

Where ϕ is the porosity, r is the distance from selected center point, and s is the specific surface area (internal surface area per unit volume). The 2.5 depth averaging technique ensures that no solid or void voxel is replaced or removed, and therefore, $S_2(0) = \phi$ remains valid. What can be significantly affected by the depth averaging technique is $S_2'(0)$. For large depth averages, one would expect the probability of finding void voxels in the immediate vicinity of a randomly selected void voxel to be significantly higher. The result is a two-point correlation function with a more gradual decline. For lower depth averages, the two point correlation function should not deviate. As more layers are added, however, one should expect *s* to be smaller in magnitude.

Algorithm

The two-point correlation function itself can be calculated from either a two dimensional scan for 2-D slices or a three dimensional scan for 3-D structures of the same material so long as it is isotropic and homogenous. Therefore, when using the two point correlation function as a variable to either generate a 3-D artificial porous media from a 2-D slice (Hidijat, 2002) or inversely as a variable in generating a 2-D micromodel from 3-D image, the algorithm can be switched to either two or three dimensions. This is not the case in our 2.5-D micromodels.

Additionally, the boundary layers on the side and top of the micromodel play a crucial role for the micromodel design by enclosing the pore from above. It must therefore be considered as part of the solid space to be scanned. This presents a fundamental problem by adding at least an entire outside perimeter's worth of voxels to the scanning algorithm. This results in a reduced calculated porosity in the system for the standard algorithm.

To correct for this, we limit the search of point r_0 to the void space. We separately calculate the porosity, and multiply this back into the two point correlation function search to obtain the same information as was produced by a scan of all voxels in the structure.

The size of the system's outer solid boundary is another point to be determined. In comparing these micromodels to the full 400-voxels^3 image, it may be reasonable to ensure equal dimensions of the micromodel to the full image. Therefore, for our analysis, additional solid layers were added to either side of the micromodel until the vertical size reached 400 voxels. The expected result of this change is that $S_2(0)$ will remain the same, but the addition of the outer layer will lower $S_2(r)$ as it approaches infinity, and will be more significant for very low depth averages.

3.3.4 Chord Length Distribution Function

The chord length distribution is the probability $p(x)$ of finding a chord of length between x and x + dx entirely within a single phase of a two-phase system. The chord length distribution also relies on the assumptions that the porous media is homogenous and isotropic; however, the chord- length distribution is more strongly affected by the depth averaging technique because the algorithm itself relies significantly on the two assumptions.

Though an infinite number of lines can be placed through a single point, the algorithm to obtain the chord-length distribution from a voxel image scans the orthogonal directions of the system. This will affect the vertical direction chord length distribution but is actually beneficial for optimization. For a depth average smaller than the average pore size, the z-direction chord distributions will at most produce chords equal to the total depth of the micromodel, thereby increasing the probability distribution of smaller chords. On the contrary, at significantly large depth averages larger than the average pore size, multiple layers of porous regions are joined together, skewing the distribution to have a higher probability of lengthier chords. The sum of squares difference between the 2.5-D micromodels and the original 3-D structure should give a good indication of the ideal depth average.

Algorithm

The algorithm for the chord length distribution is also simple. In each orthogonal direction x, y, and z, a scan begins at (0,0,0) and systematically scans an entire line. The algorithm scans for the solid/void interface, counts the voxel length until reaching the next interface, and stores the information to formulate the distribution. When a line is complete, the scan shifts to the next; once the entire cross section is complete, the process repeats for the next cross section.

3.3.5 Minkowski Functionals

The Minkowski functionals are a set of four morphological measures obtained from integral geometry that describe the shape and connectivity of the image. Specifically, for three-dimensional objects, the four functionals correspond to the enclosed volume, surface area, mean-breadth, and connectivity (Euler Characteristic) of the system.

The natural sensitivity of the Minkowski functionals to closely similar structures have made them useful for statistically quantifying complex patterns, and measuring small changes of such complex patterns over a spatial or temporal period. A summary of the potential applications of the Minkowski functionals is outlined by Mecke (2000), which include characterization pattern transitions in dissipative systems, spinodal decomposition, or to characterize the atomic structure of simple fluids. Its use as a dynamical quantification of pattern transition has been extensively studied in the porous media community as a means to characterize porous media (Blasquez & Pouraudeaux, 2003); (Lehmann, 2008), reconstruct porous media models that replicate previously characterized rocks (Mecke & Arns, 2005), and to predict phase distribution and flow behavior in porous media (Mecke and Arns, 2003); (Vogel, 2002); (Lehmann, 2008).

Significant changes in the structure occur in the transition from the 3-D porous media to 2.5-D micromodels. The sensitivity of the upper order Minkowski functionals to just small changes of the porous media translates to massive changes in the higher order Minkowski functionals. Lehmann (2008) describes the meaning of the 2^{nd} order Minkowski functional, the mean breadth (proportional to the integral mean curvature), as reliant on the curvature of the structure. A complex network containing convex structures will have a negative mean breadth. For the 3^{rd} order Minkowski functional, the Euler characteristic, highly connected networks with redundant connections give a negative value, and positive for isolated elements.

The calculations of the Minkowski functionals for a porous media voxel image are essentially summations of the number of void voxels and their free faces, edges, and vertices. For the volume (M_0), a simple count of the total void voxels gives the overall void space, while dividing it by the overall number of voxels gives the porosity. This should be identical for the 2.5-D micromodels, since the depth averaging technique does not change the voxel phase. The surface

area (M_1), mean breadth (M_2), and connectivity (M_4), however, are drastically altered during the transition. Examining Figure 14 (from DeReadt), depicts how drastic the Euler characteristic changes based on the absence or presence of a void "hole". A solid, convex cube has an Euler characteristic of +1, a cube with a path through the structure has an Euler characteristic of 0, and two separate void paths connected by an edge, -1. The local sensitivity of these Minkowski functionals is cumulative for the entire network.

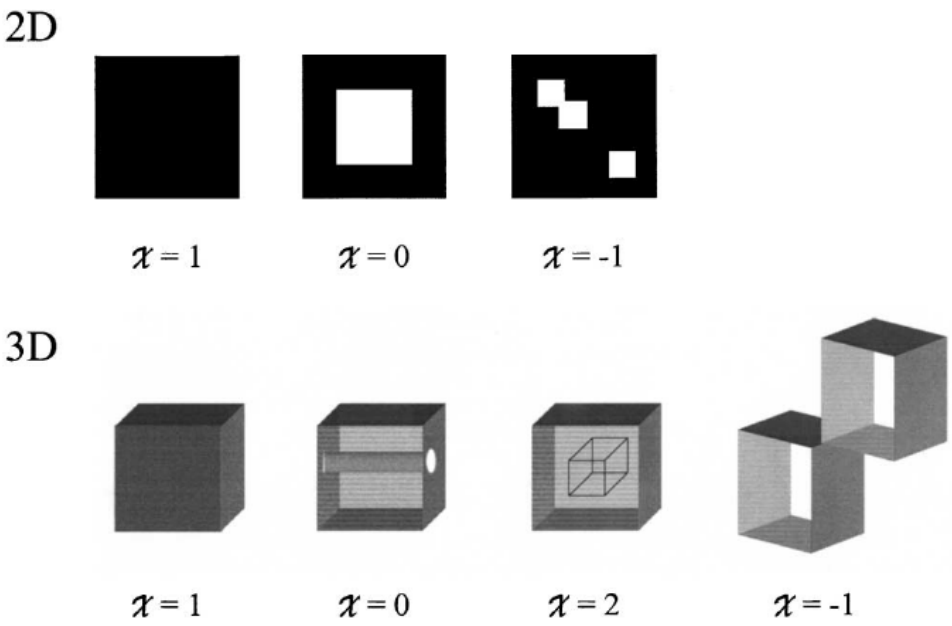

Figure 11. Two- and three-dimensional figures with various connectivity numbers or Euler characteristics χ. As taken from Michielsen and De Raedt, Physics Reports 347, (2001), pg. 487.

3.3.6 FEM Simulation

Stokes-flow FEM simulations can be used to obtain local pressure and velocity information throughout the porous media system. This information, particularly the velocity data, is important in order to understand and quantify the transition from the 3-D structure to 2.5-D

micromodel for two reasons. First, the vertical direction velocity distribution will indicate if 3-D flow behavior is induced; second, velocity distributions will be used to quantify and optimize the number of voxel layers to depth average to best match the velocity distributions of flow in the actual pore structure.

Algorithm

Details on the Stokes flow finite element model used for these experiments can be found in the dissertation "Numerical Studies of Flow in Porous Media Using an Unstructured Approach" by Nathan Lane. Given a pore-scale 3D description of a porous medium, CFD simulations can be used to obtain local pressure and velocity throughout the pore space.

In this work, we performed single-phase fluid flow simulations by creating a mesh from the voxelized imaged using a CAD-based approach (AVIZO® software). This approach constructs an isosurface of the original voxel image and uses an advancing front algorithm to fill the void space with tetrahedral elements of a desired size range. To ensure comparability during the optimization process, all parameters and steps in the mesh generation were identical for each depth averaged micromodel design.

We use an in-house Stokes flow simulator. The mesh is exported from AVIZO using the Hypermesh format and converted to our in-house format meshing format. This allows us to apply boundary conditions and node types for each node of the mesh. No-slip boundary conditions are placed on all of the solid-void surface nodes while specified traction boundary conditions are imposed at the inlet and exit nodes. The FEM solver employs P_2P_1 elements, and the pressure and velocity fields are solved simultaneously using a mixed-method approach. Once completed the nodal velocity and pressure are converted back to voxel-based information to homogenize the

spacing of the data and to visualize fluid streamlines. The voxel velocity data are used to generate x, y, and z velocity distributions, which allow comparison of the 3D and 2.5D flow fields using a sum of squares error analysis (for which error is composed directly from the scalar values.

The Stokes flow code initially simulates non-dimensional flow through the image, and scaling the accumulated information to actual sizes is reliant on the length scale of the XMCT image. For flow across a mesh, the entrance and exit hydrostatic pressures are set as boundary conditions, neglecting the velocity gradient contribution. Although the permeability gives important insight, velocity distributions provide a more fundamental understanding of how well the micromodels reproduce flow behavior at a local level, while also allowing us to quantify whether they are able to induce flow in the third dimension. Since the pressure is kept constant across the direction of flow for all of the simulations, velocities are normalized with Darcy velocity in each simulation. This approach allows us to compare permeability (see previous section) independently of how well local flow patterns are reproduced.

3.3.7 Permeability

After the pressure gradient, nodal velocities, and total flow rate across the porous media are obtained from the simulation, the permeability can be calculated. The permeability is directly related to the velocity through the Darcy's law, and is a scalar representation of the integrated velocity distribution. It is a useful descriptor of porous media, and will be considered in conjunction to the velocity distributions in determining the final optimum thickness of the micromodel.

CHAPTER 4 RESULTS AND DISCUSSION

Materials and Methods

We show a rock-based micromodel pattern created from a Boise sandstone core, which was supplied by Prof. Steven Bryant at the University of Texas in Austin. Imaging was performed at the Center for Advanced Microstructures and Devices at LSU at 5.07 micron/voxel resolution. The image was segmented and a 400^3 voxel section (2.03mm×2.03mm×2.03mm) section was extracted for generating the micromodel. Depth Averaging was performed over a range of 5 to 500 μm, or 1 to 99 voxels,

An array of data was obtained for each depth averaged micromodel design and compared to that of the original Boise structure. Morphological data obtained from the network models, including the pore coordination number, inscribed pore diameter, inscribed pore volume, inscribed pore-throat diameter, pore-throat aspect ratio, throat length, and hydraulic conductivity were obtained for each pore and throat in the network. Stochastic distributions including the two-point correlation function and chord-length distribution function were compared. Capillary pressure curves from quasi-static drainage simulations were compared. Finally, a number of single-phase flow data (from simulation) were compared, including permeability and velocity distributions for each micromodel in the three coordinate directions: the direction of flow (x), the transverse (y) and vertical (z).Each parameter distribution was compared to the original using a sum of squares error analysis, with the exception of the scalar permeability data.

4.1 Network Morphology Results

4.1.1 Overview and Results Table

Table 1. Sum of squares error analysis for 2.5-D micromodels- pore-network statistics.

DEPTH		NETWORK STATISTICS- PORE DATA SSE				NETWORK STATISTICS- THROAT DATA SSE			
(Voxels)	(µm)	Pore Coordination Number	Inscribed Pore Diameter	Inscribed Pore Volume	Inscribed Pore-Throat Diameter	Pore Throat Equivalent Diameter	Throat Aspect Ratio	Throat Lengths	Throat Conductivity
5	25.35	0.061	0.1348	0.0006	0.0553	0.0356	0.0499	0.046	0.017
7	35.49	0.022	0.0625	0.0003	0.0223	0.0069	0.0221	0.015	0.009
11	55.77	0.001	0.0359	0.0003	0.0063	0.0025	0.0184	0.009	0.004
15	76.05	0.001	0.0273	0.0005	0.0028	0.0052	0.0258	0.007	0.002
19	96.33	0.005	0.0452	0.0022	0.0074	0.0137	0.0286	0.012	0.003
23	116.61	0.013	0.0453	0.0065	0.0106	0.0136	0.0267	0.015	0.003
27	136.89	0.017	0.0460	0.0064	0.0166	0.0210	0.0273	0.016	0.004
31	157.17	0.018	0.0545	0.0091	0.0117	0.0185	0.0326	0.015	0.004
35	177.45	0.022	0.0579	0.0102	0.0171	0.0224	0.0311	0.016	0.004
39	197.73	0.026	0.0634	0.0170	0.0218	0.0282	0.0302	0.022	0.005
43	218.01	0.030	0.0629	0.0212	0.0150	0.0277	0.0365	0.017	0.005
47	238.29	0.043	0.0693	0.0248	0.0272	0.0355	0.0366	0.026	0.009
51	258.57	0.046	0.0775	0.0334	0.0269	0.0354	0.0372	0.022	0.007
55	278.85	0.059	0.0866	0.0441	0.0336	0.0430	0.0410	0.028	0.010
59	299.13	0.068	0.0993	0.0517	0.0457	0.0500	0.0373	0.034	0.012
63	319.41	0.079	0.1009	0.0551	0.0479	0.0507	0.0367	0.034	0.013
67	339.69	0.084	0.1159	0.0634	0.0502	0.0524	0.0384	0.037	0.016
71	359.97	0.079	0.1058	0.0726	0.0431	0.0450	0.0472	0.031	0.014

Table 1 displays comparisons of the 2.5D micromodels to the 3D Boise sandstone, for depth averaged micromodels between 25 µm (5 voxels) and 360 µm (71 voxels). The values shown in the table are the absolute error for scalar parameters or the sum-of-the squares error for distributions. In all cases, these are for computationally determined parameters in both the micromodel and the original rock. For most of the compared parameters, clear minimums in the error occur, which that indicate an optimized depth average. While each of parameters displays a slightly different optimum, the general region between 55 to 177 µm displays relatively low errors over a wide range of parameters.

Using the error analysis to help interpret physical changes between micromodel designs suggests which parameters could be more significant in the optimization process. One such network parameter is the pore coordination number. The distribution offers insight into the connectivity of the porous medium.

4.1.2 Pore Coordination Number

The pore coordination number is the number of other pores directly connected to the given pore. The distribution offers insight into the connectivity of the porous medium. Figure 12-(a) shows the distribution for the Boise sandstone network.

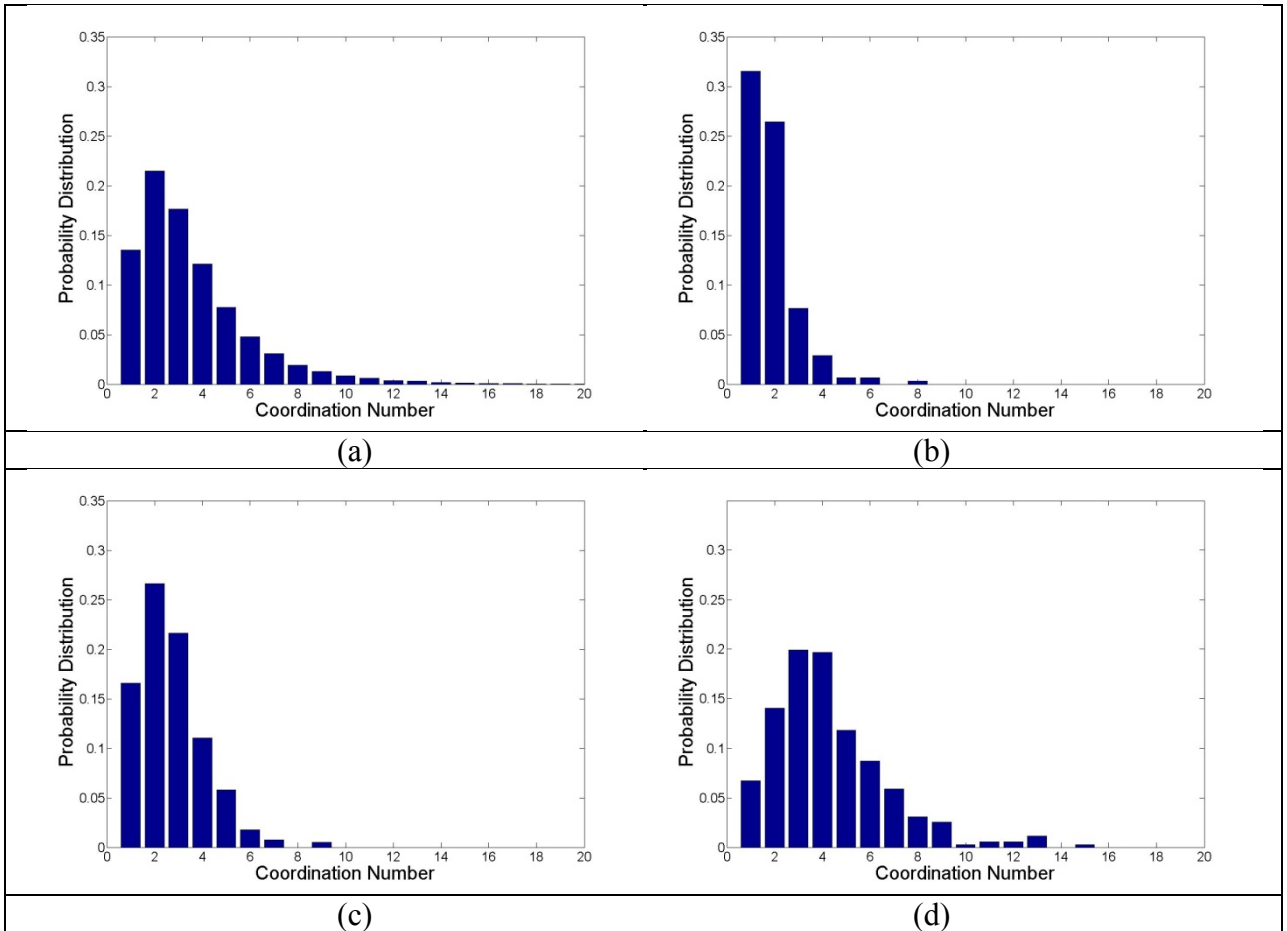

Figure 12. Pore coordination numbers for (left to right, top to bottom): Original Boise sandstone, 5-Voxel Depth Average (VDA), 15-VDA, 71-VDA

Figure 12 displays the pore coordination number distributions of networks generated from the original Boise sandstone (a), depth average of 25- (b), 86- (c), and 360-microns (d) deep. A lack of connectivity for smaller depths can be seen for the 25 µm depth average distribution, which shows that more than 90% of its pores are connected to two pores or fewer. On the other end of the spectrum, the large depth average displays a normal distribution with considerably more pores with high connectivity. For the network generation, this represents the presence of large pore spaces linking to a large number of smaller neighbors.

Physically, these trends indicate a phenomena in which overlapping, unconnected void voxels are pushed down between pores previously separated by a solid barrier in the vertical direction, thus creating a connection not previously there.

Figure 13 displays the sum of squares error between each micromodel network and the original Boise sandstone network for depth averages of 5 to 71 voxels (5 to 360 µm). The pore coordination number distributions predict an optimum near 17 voxels (86 µm) and an optimum range between 15 to 31 voxels (76 to 157 µm) in depth.

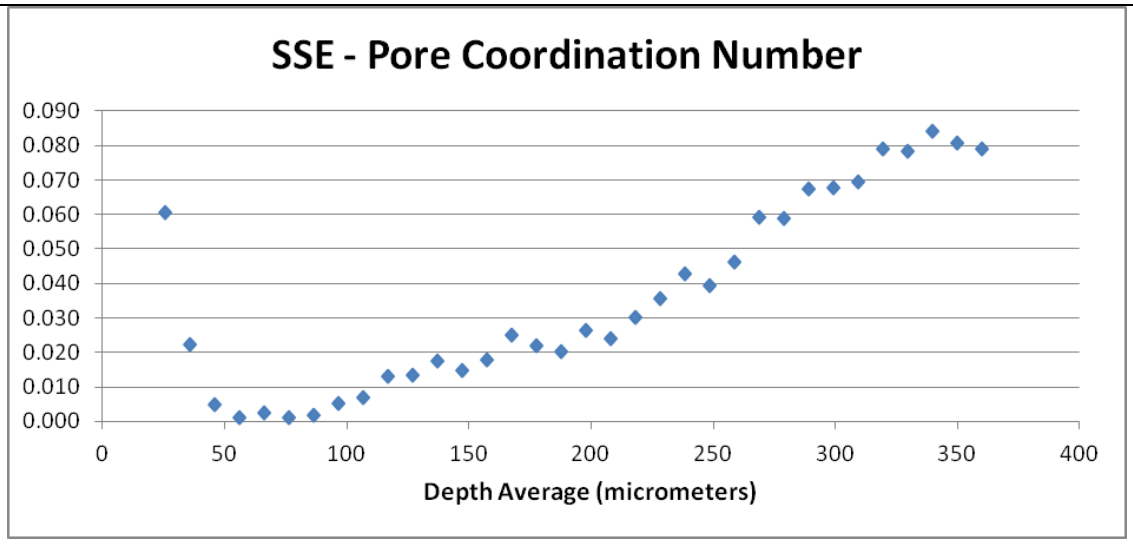

Figure 13. Sum of squares error for pore coordination numbers at various depths.

4.1.3 Inscribed Pore Diameter

Another parameter, the inscribed pore diameter, is used to construct a pore-size distribution for the structure. Because the pore-size distribution requires a three-dimensional image (Coker & Torquato, 1996), depth averages ranging from a single image slice of 5 microns to as high as 25-micron depth averages (5 voxels) obtained a high degree of error. These depths had no connectivity of the pore space across the micromodel, and thus no permeability, as will be shown later. In Figure 14, the inscribed pore diameter indicates an optimum region of 55-100 microns.

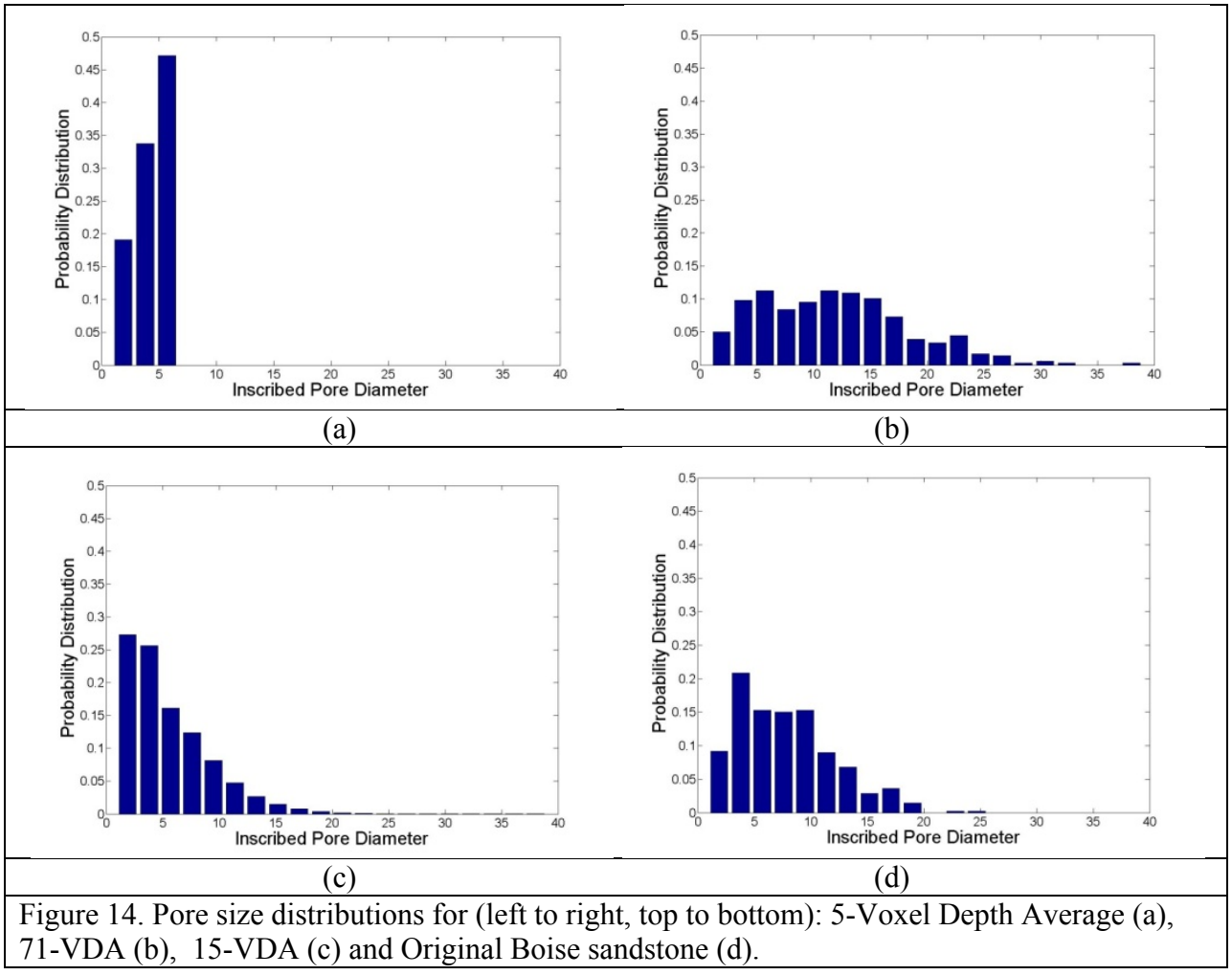

Figure 14. Pore size distributions for (left to right, top to bottom): 5-Voxel Depth Average (a), 71-VDA (b), 15-VDA (c) and Original Boise sandstone (d).

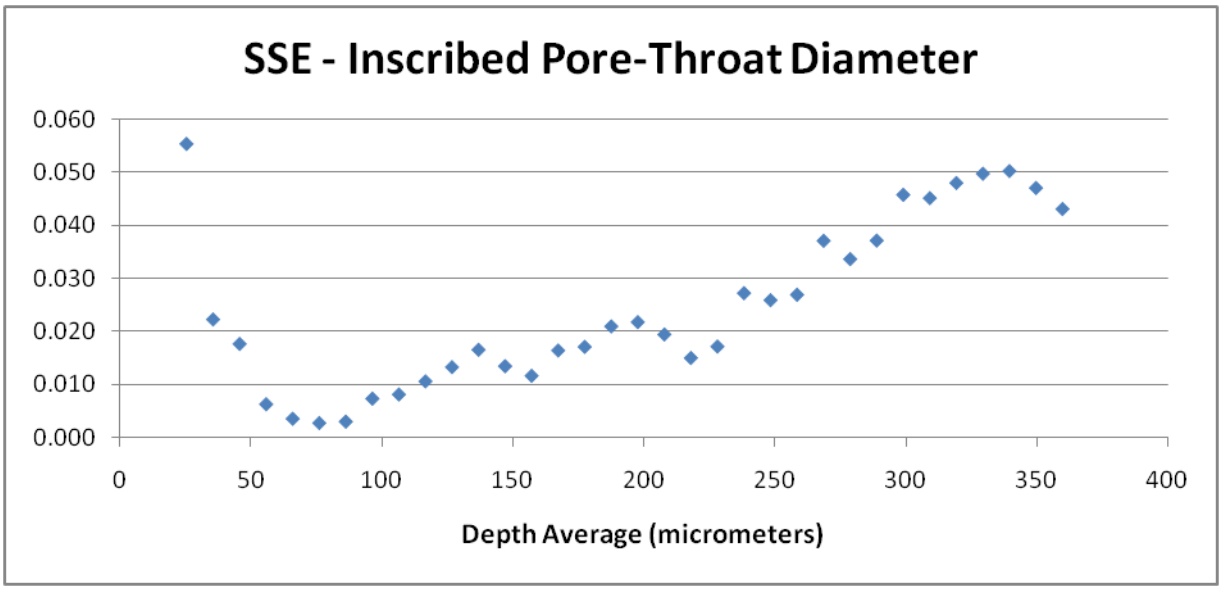

Figure 15. Sum of squares error for the inscribed-pore throat diameter at various depths.

4.1.4 Hydraulic Conductance

The hydraulic conductance is used in network modeling to determine the local flow rate between two pores, and is a function of the local pore geometry. Our network models calculate the hydraulic conductance $g_{i,j}$ between two pores *i* and *j* using an equation developed by Thompson and Fogler (1997) that is a function of pore-throat radius, throat length, and pore-throat aspect ratio.

Because of its reliance on pore-size distribution as well as its relevance to permeability and connectivity, one would expect the hydraulic conductivity to display reasonable correlation to the ideal depth average. The figure above indicates a wide optimum range between 45 µm to 126 µm.

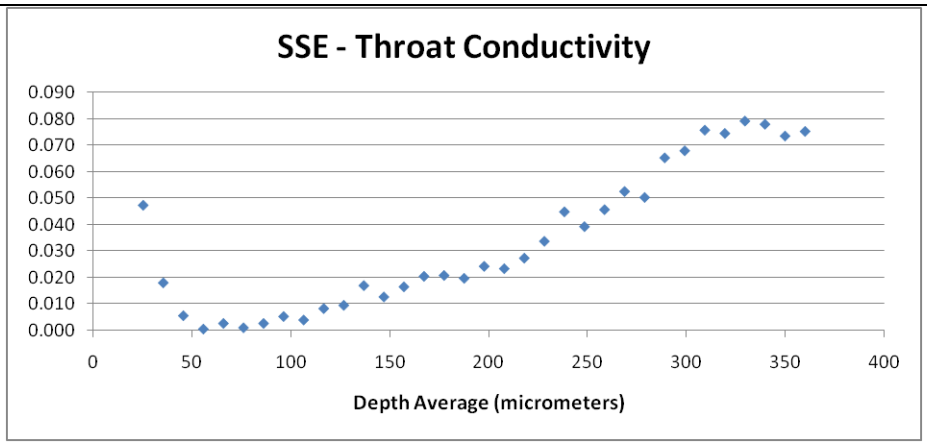

Figure 16. Sum of squares error for the hydraulic conductance at various depths.

4.2 Statistical Correlation Results

Depth averaging renders the distribution of solid voxels higher at lower depths, and inversely lower at the top of the micromodel. This will affect the two-point distribution function and chord length function. However, the purpose of these two distributions is to determine at which depth average the micromodels' distributions best match the original structure. In fact, the problems of local isotropy and homogeneity are both exacerbated at extremities of depth averaging, allowing these functions to give an indication as to where the optimum depth average lies.

4.2.1 Two-Point Correlation Function Distribution

As stated in Chapter III, the micromodels were given additional solid layers above and below the original region until each height reached 400 voxels. The average pore diameter for the original Boise sandstone image is 5.6 voxels. Regarding the function, Figure 17 indicates the minimum is reached within 50 voxels.

φ=.19

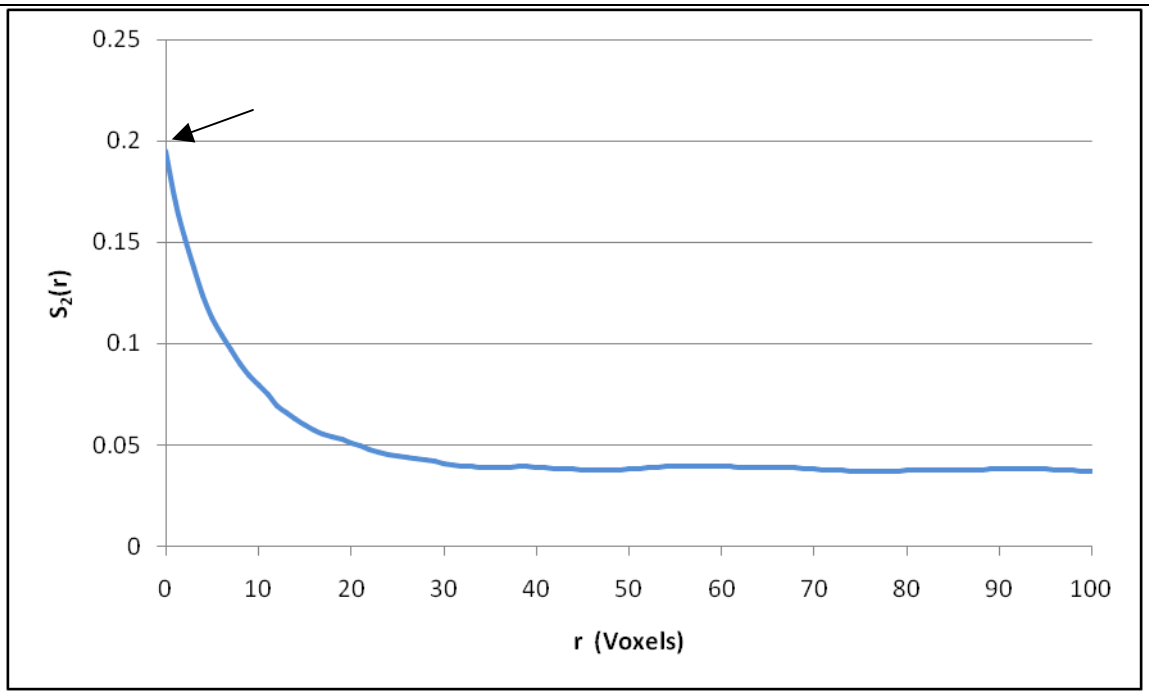

Figure 17. Two point correlation function (S_2) for the original Boise sandstone image. *r* is measured in voxels.

Figure 18-(a) and 18-(b) display the results for multiple depth averages, shown at different magnitudes **r** from the seed point to illustrate the curvature of the depth averages. The effects of the added layers are apparent. While the function for the Boise sandstone approaches φ^2, those of the depth averaged micromodels approach zero. On the other side of the spectrum, we look to see how the addition of these boundaries affects the region immediately surrounding the seed voxel. Though we cannot make observations on the intercept due to the algorithm's direct reliance on φ, we can make observations on its effects of $S_2'(0)$. Figure 19 displays the difference in the specific surface area [μm^{-1}] calculated using the two point correlation function. One can conclude in Figure 19 that too small a depth reduces the probability of finding void space near the origin and alternately too large a depth average increases the probability of finding void. This

is directly related to the depth averaging phenomena regarding the addition of overlapping, unconnected void spaces.

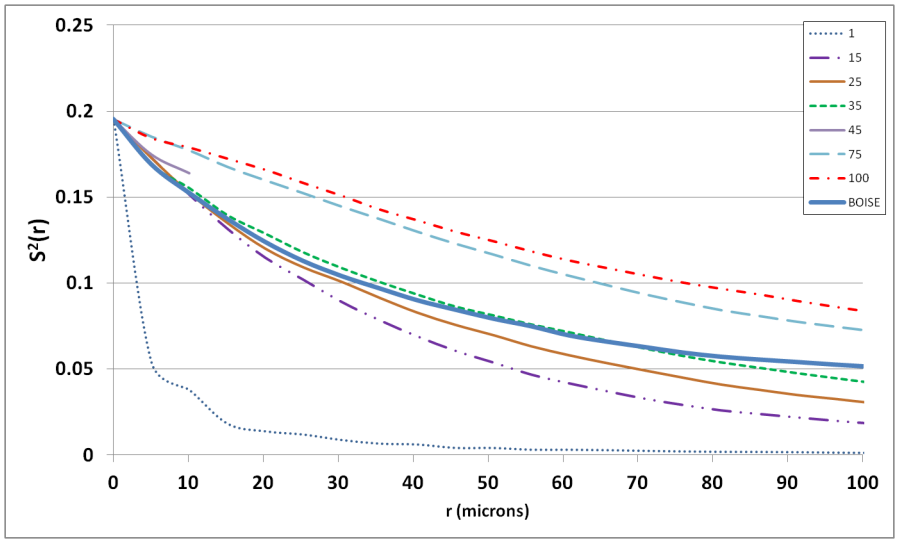

(a)

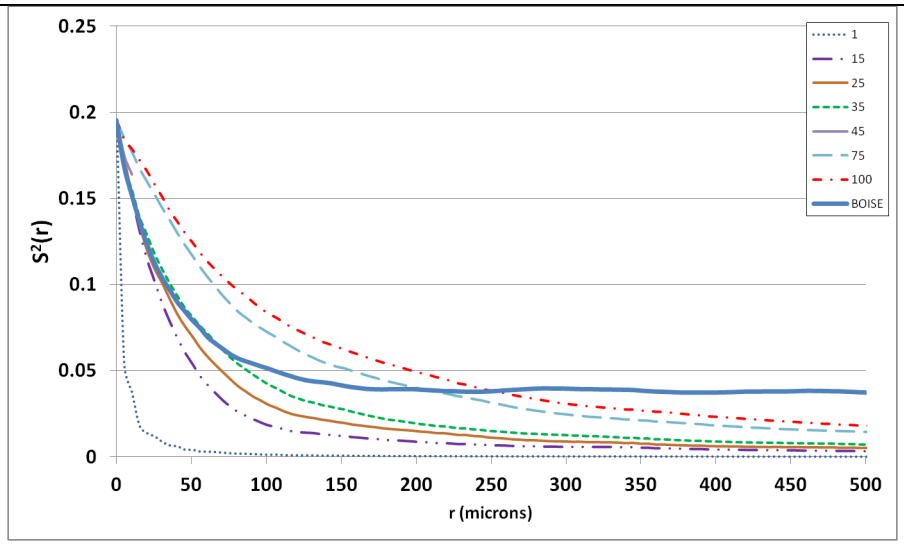

(b)

Figure 18. Two point correlation functions for multiple depth averages, within 20 voxels (100 μ, above) and 250 distance.

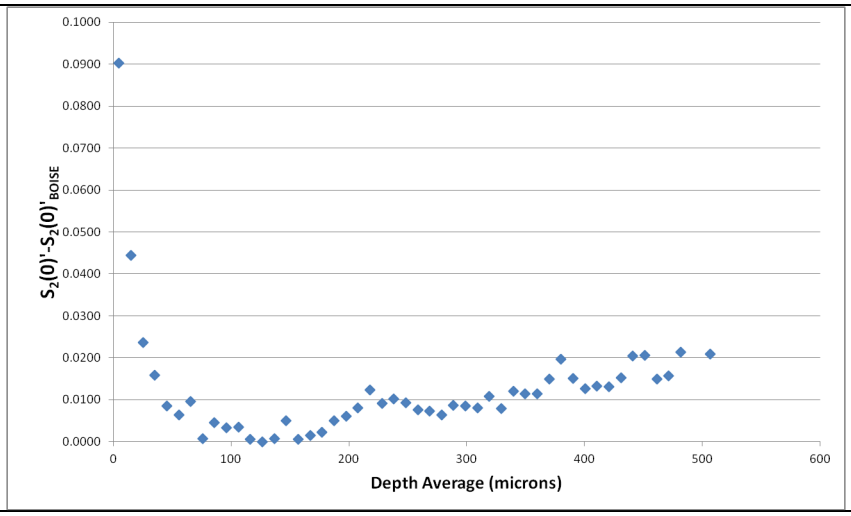

Figure 19. Sum of squares error of the calculated specific surface area, $S_2(0)'$, or *s*

While the differences in the two point correlation function can be explained, and insight to the optimum depth average can suggested, the use of the two point correlation function is still questionable. The effect of the selected magnitude over which to compare the functions to the original is apparent in Table 2.

4.2.2 Chord Length Distribution

The chord length distribution is the probability of finding a chord of length z + dz entirely within a single phase of a two-phase system. Unlike the two point correlation function, the scan conducted and the data obtained is wholly dependent on the phase of interest and therefore will not be affected by the presence of a solid border of any size. Thus, comparisons between the micromodel and original Boise sandstone images can be quantified by a total distribution comparison. A look at the chord length distributions in the vertical direction, such as those shown in Figure 20 for depth averages of 5 and 25 voxels, shows that the distribution is affected by the total depth.

Table 2. Sum of squares analysis for the two point correlation function for five different lengths of analysis (voxels).

2-Point Correlation Function						
Voxel Depth	SSE (500)	SSE (100)	SSE(35)	SSE (20)	SSE (10)	SSE (5)
1	0.8281	0.2531	0.1523	0.1331	0.0990	0.0628
3	0.7633	0.1927	0.0957	0.0782	0.0493	0.0232
5	0.7277	0.1614	0.0683	0.0524	0.0275	0.0090
7	0.7018	0.1397	0.0502	0.0358	0.0155	0.0038
9	0.6790	0.1210	0.0354	0.0226	0.0071	0.0011
11	0.6663	0.1122	0.0305	0.0188	0.0052	0.0007
13	0.6558	0.1056	0.0280	0.0174	0.0054	0.0013
15	0.6421	0.0960	0.0214	0.0119	0.0025	0.0003
17	0.6312	0.0887	0.0172	0.0087	0.0013	0.0001
19	0.6209	0.0819	0.0137	0.0065	0.0008	0.0000
21	0.6120	0.0764	0.0110	0.0045	0.0003	0.0001
23	0.6023	0.0709	0.0088	0.0032	0.0003	0.0000
25	0.5945	0.0671	0.0074	0.0028	0.0003	0.0000
27	0.5870	0.0631	0.0061	0.0022	0.0003	0.0000
29	0.5795	0.0594	0.0046	0.0013	0.0002	0.0002
31	0.5723	0.0554	0.0036	0.0010	0.0001	0.0000
33	0.5657	0.0522	0.0026	0.0005	0.0000	0.0000
35	0.5591	0.0489	0.0018	0.0003	0.0001	0.0001
37	0.5540	0.0473	0.0020	0.0008	0.0006	0.0003
39	0.5498	0.0461	0.0024	0.0013	0.0011	0.0005
41	0.5453	0.0452	0.0031	0.0022	0.0018	0.0009
43	0.5403	0.0433	0.0038	0.0031	0.0026	0.0014
45	0.5340	0.0400	0.0028	0.0024	0.0019	0.0009
47	0.5298	0.0389	0.0037	0.0035	0.0028	0.0013
49	0.5259	0.0383	0.0048	0.0046	0.0034	0.0013
51	0.5225	0.0389	0.0069	0.0068	0.0046	0.0015
53	0.5186	0.0381	0.0079	0.0078	0.0052	0.0016
55	0.5138	0.0372	0.0084	0.0084	0.0056	0.0014
57	0.5089	0.0346	0.0078	0.0076	0.0048	0.0014
59	0.5046	0.0331	0.0080	0.0078	0.0047	0.0013
61	0.5005	0.0327	0.0091	0.0087	0.0046	0.0013
63	0.4999	0.0352	0.0125	0.0118	0.0067	0.0022
65	0.4939	0.0332	0.0110	0.0102	0.0052	0.0015

Figure 20(a) indicates that 44% of the void voxels are part of a chord length of equal to the maximum length in the z-direction. This effect is less severe but still visible for the 25-voxel micromodel depth average in Figure 20(b). These features are best displayed by the x-direction and z-direction figures for a micromodel with only a single slice displayed in Figure 18.

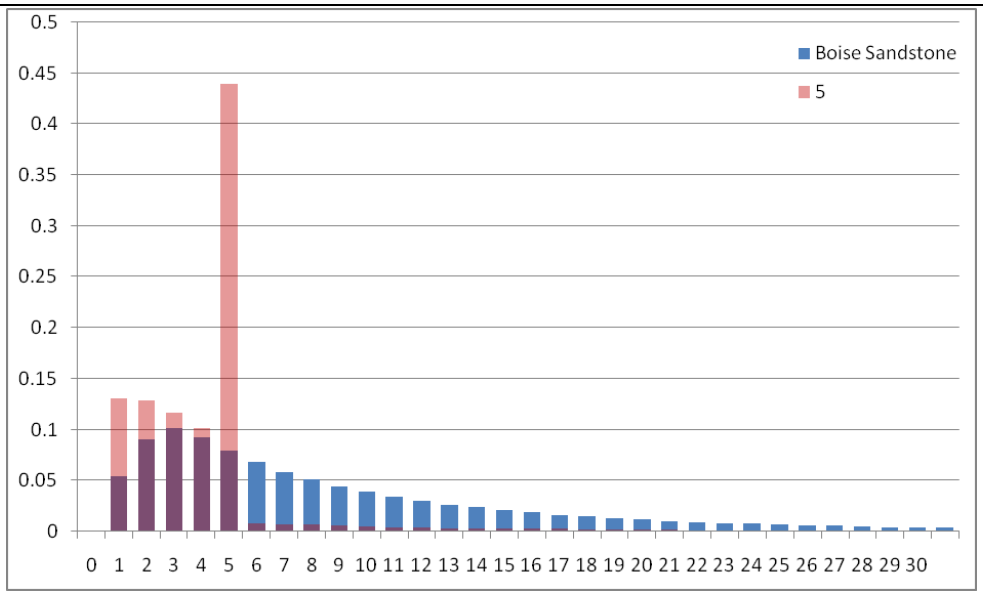

(a)

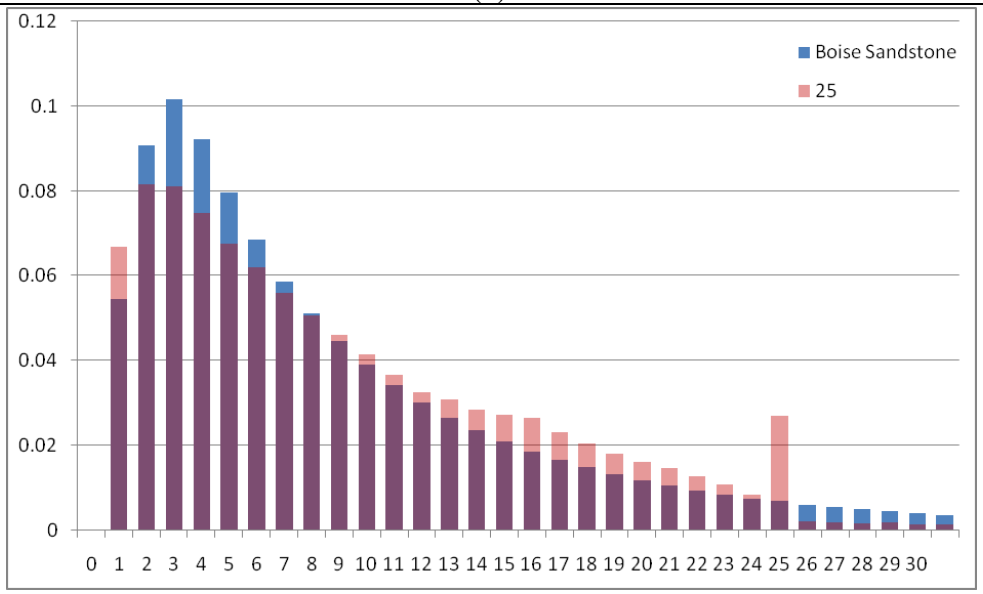

(b)

Figure 20. Chord length distributions in the z-direction of the 5- (a) and 25- (b) voxel depth average as compared to the Boise sandstone distribution.

Figure 21 shows the chord length distributions in the x-direction. The 5-voxel depth average chord length distribution displayed in Figure 21(a) displays a closer distribution to the original image than the 25-depth average in Figure 21(b), whose distribution of chords 1- voxel long are much larger than original Boise sandstone. This is a direct result of the depth averaging

algorithm. The 5-voxel depth average has a lower probability of solid voxels being moved down to the lower layers from above, and therefore has less chance of longer chords becoming shortened or disconnected. For the 25-voxel deep micromodel, the likelihood of longer chords being disconnected at the lower layers is displayed by the high probabilities of 1-voxel chords, while the possibility of creating longer chords in the higher layers increases the distribution of the micromodel to be larger than that of the original Boise sandstone image at around 25 voxels. The result is a more flattened distribution.

These subtle changes in each dimension play a substantial roll in optimizing the total chord length distribution, which combines the x, y, and z-distributions. For example, a single layered micromodel will display matching results in the x and y directions to the original structure, but, assuming it is a 3-D object, a skewed comparison in the z direction, since the height of the pores is limited to only one voxel.

Physically, these pores are not the same size as those in Boise sandstone. At the same time, the distributions for very large depth averages, such as in Figure 23, indicate that in the x-dimension scan in Figure 23(a), the lower levels include many single-voxel chord lengths while the upper have considerably long chords. Meanwhile, the z-direction scan in Figure 23(b) displays a wide distribution of longer than normal chords, indicating that a large number of normally unconnected pore regions have been joined into fewer, larger pore bodies.

The results of the optimization process can be shown in Figure 25 that displays the total (combined) chord length distributions combined for all three dimensions for depths at (a) 5-voxels, (b) 25-voxels, and (c) 64 voxels, and in Figure 26 that shows the sum of squares error

analysis. A depth of 25 to 29 voxels (125-150 μm) is the chord-length distribution-based optimum.

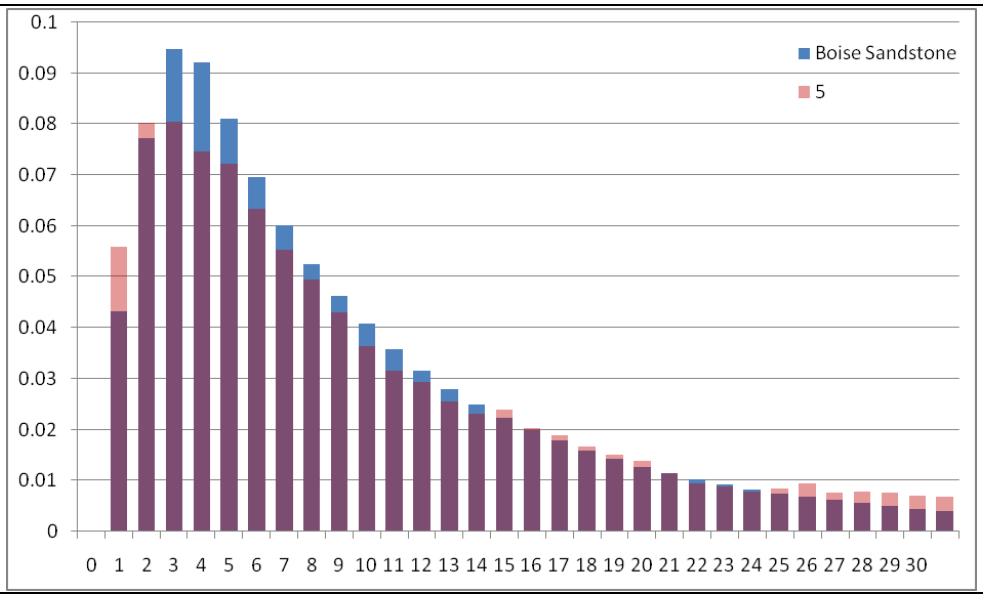

(a)

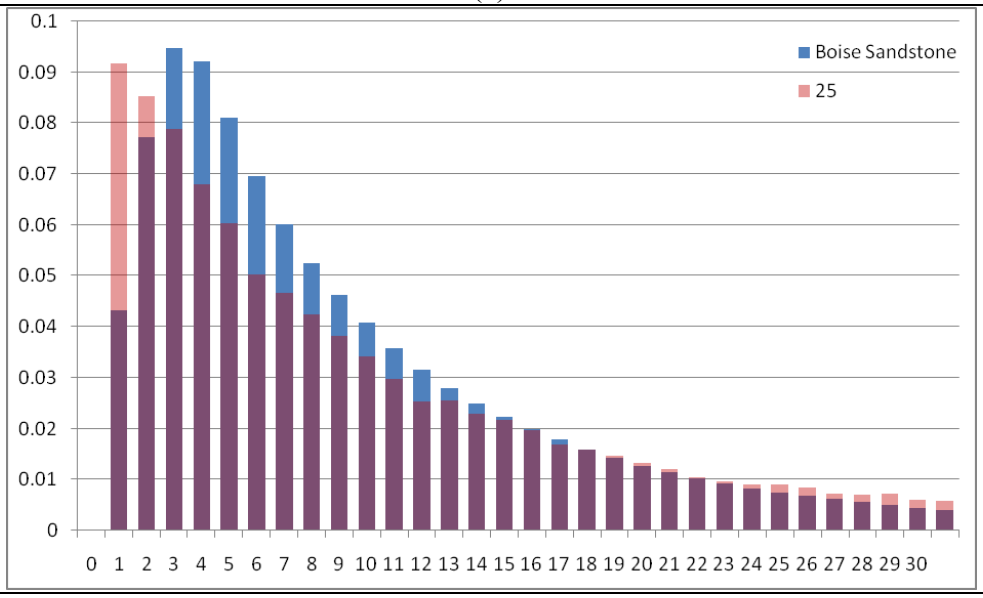

(b)

Figure 21. Chord length distributions in the x-direction of the 5- (a) and 25- (b) voxel depth average as compared to the Boise sandstone distribution.

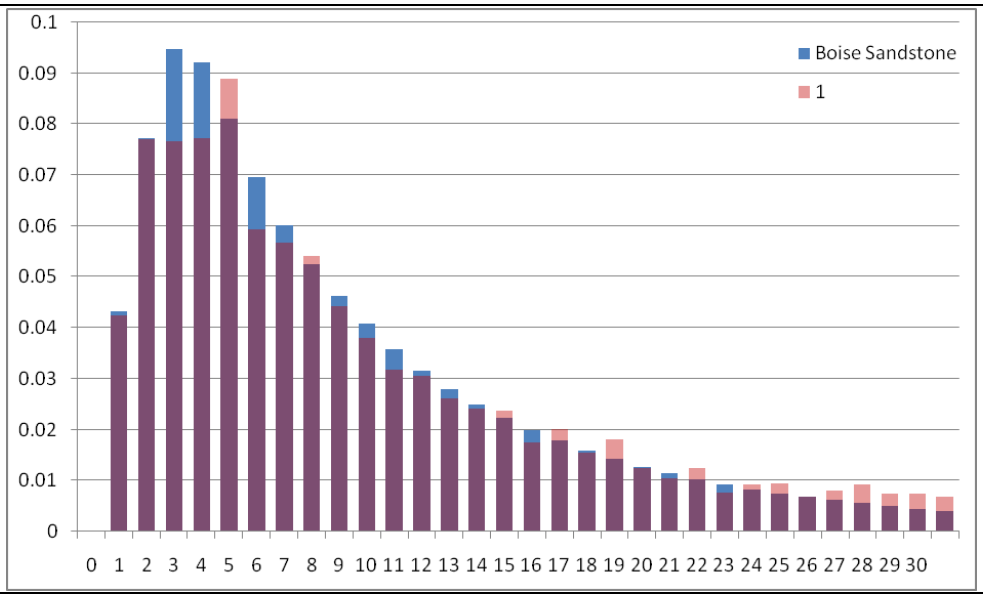

(a)

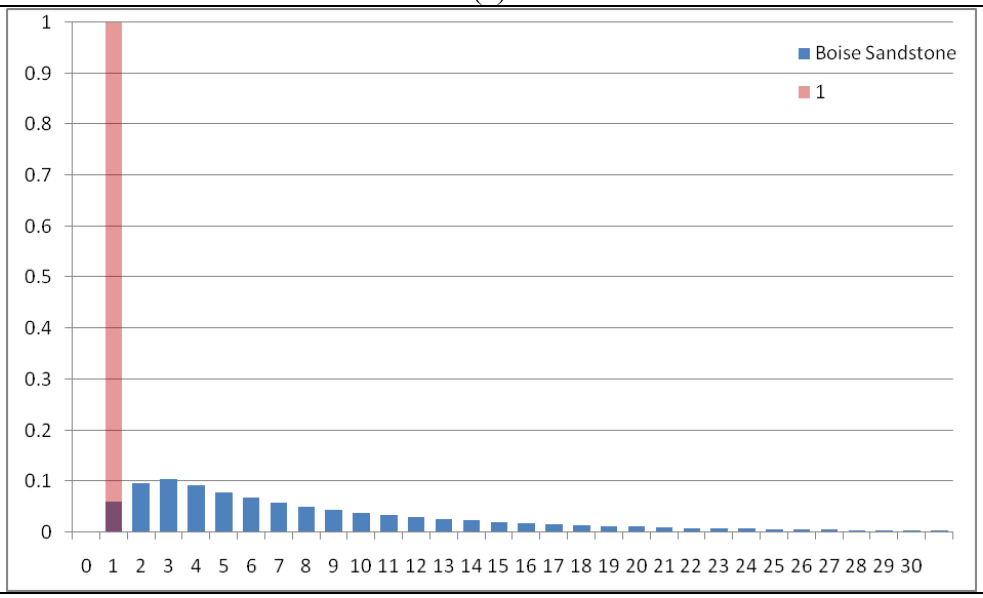

(b)

Figure 22. Chord length distributions in the (a) x-direction and (b) z-direction for single-slice micromodel.

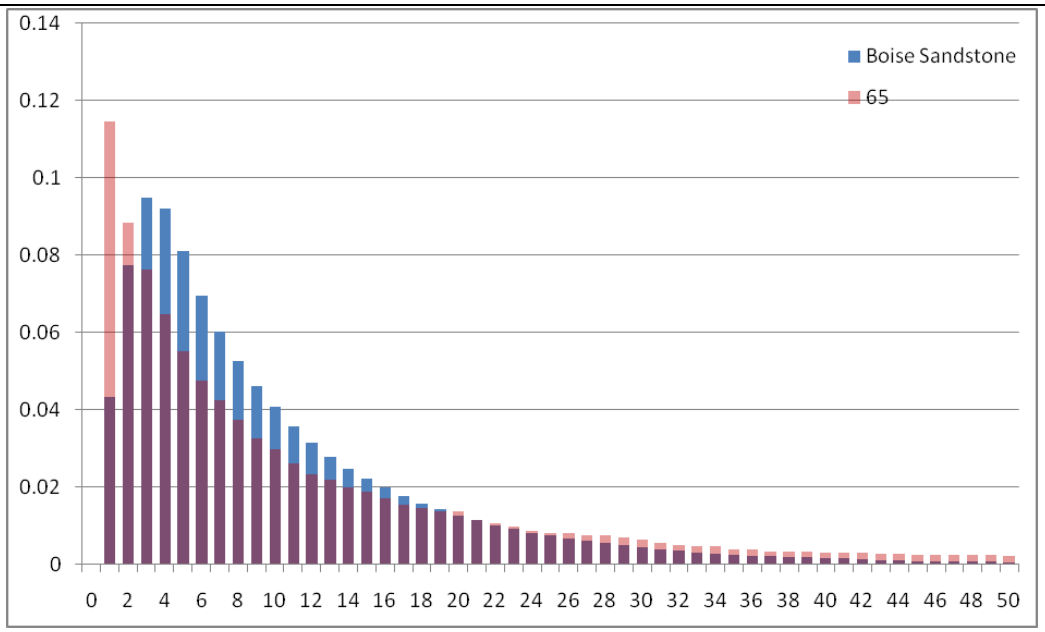

(a)

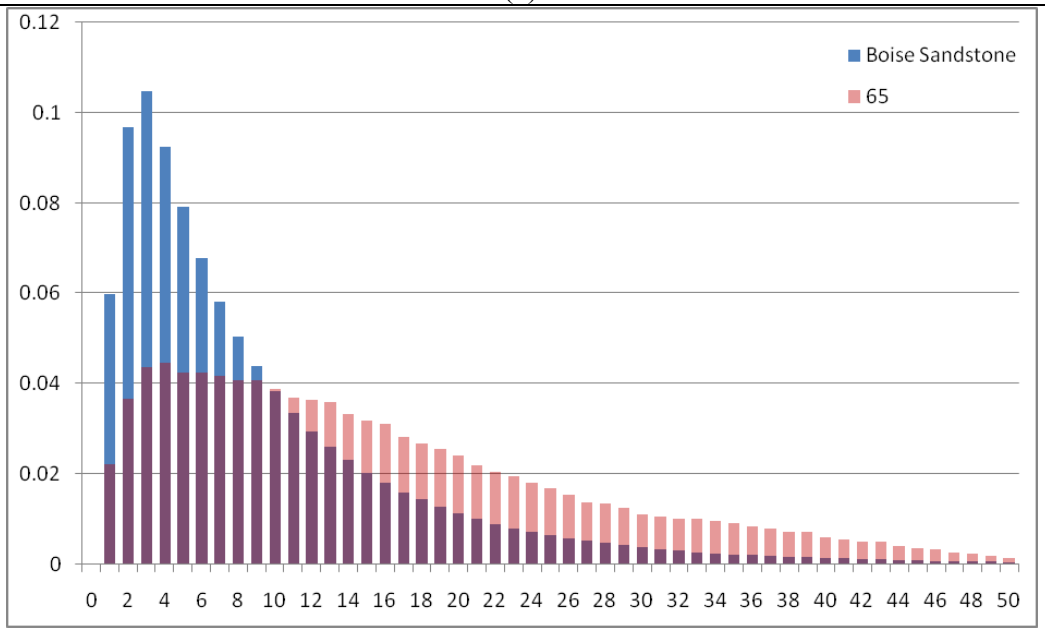

(b)

Figure 23. Chord length distributions in (a) x- and (b) z- directions for 65 voxels depth averaged micromodels.

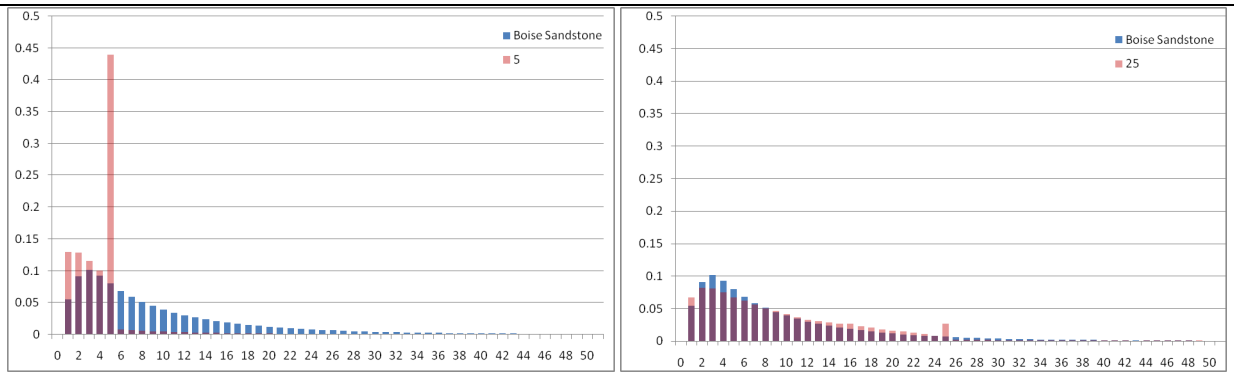

(a) (b)

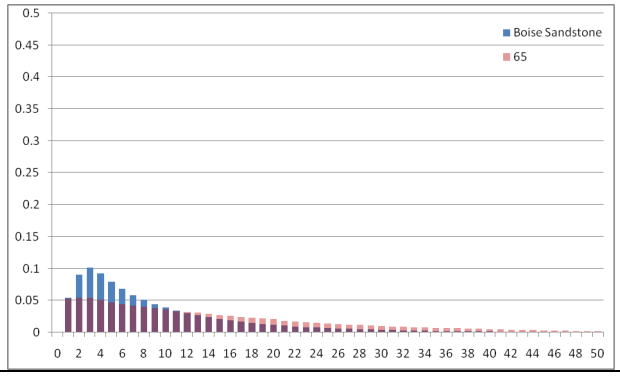

(c)

Figure 24. Total chord length distributions of all three dimensions for (a) 5-, (b) 25-, and (c) 65-voxel depth averages.

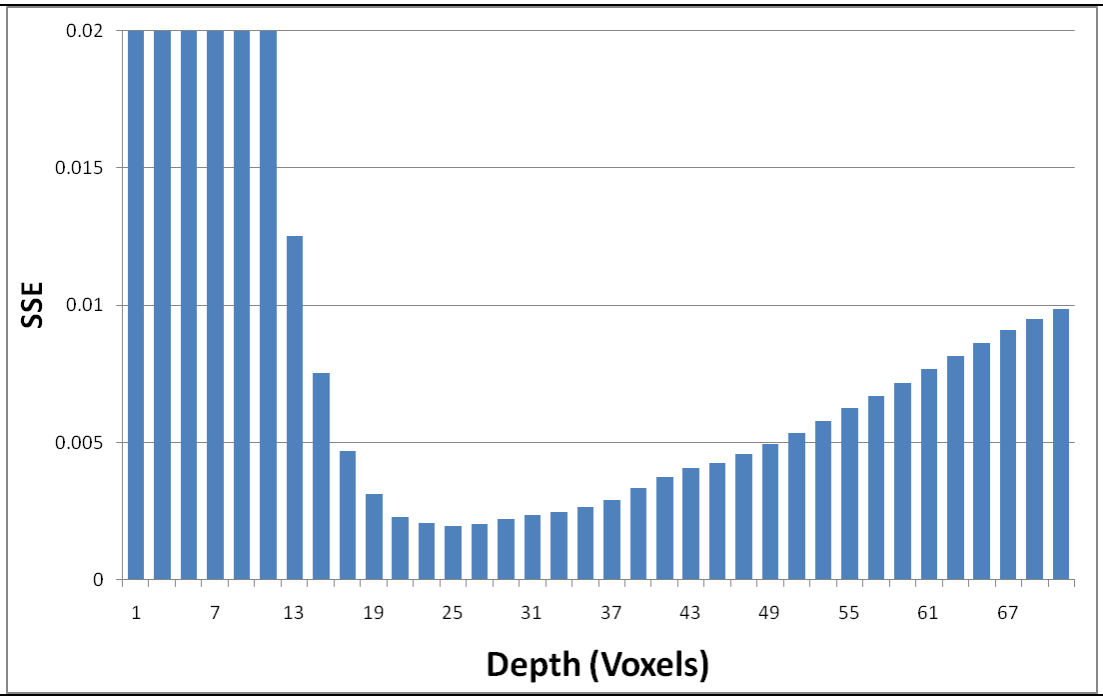

Figure 25. Sum of squares analysis of the total chord length distributions for micromodels of depths of 1-71 voxels.

4.3 Capillary Pressure Curve (CPC) Results

Figure 26 displays capillary pressure curves for the Boise sandstone and various micromodel networks obtained using Quasi-static drainage simulations. A flat curve indicates a relatively homogenous pore size distribution for the Boise sandstone CPC.

For the depth averaged pore networks, a lack of connectivity limits the saturation to 0.8 below 45-µm. Full connectivity occurs at 96 µm. The smallest error for the full saturation profile comparisons lies between 100 and 200 µm. When comparing the curve from 0-.5, a more pronounced optimum depth of 177 µm (35 voxels) is displayed.

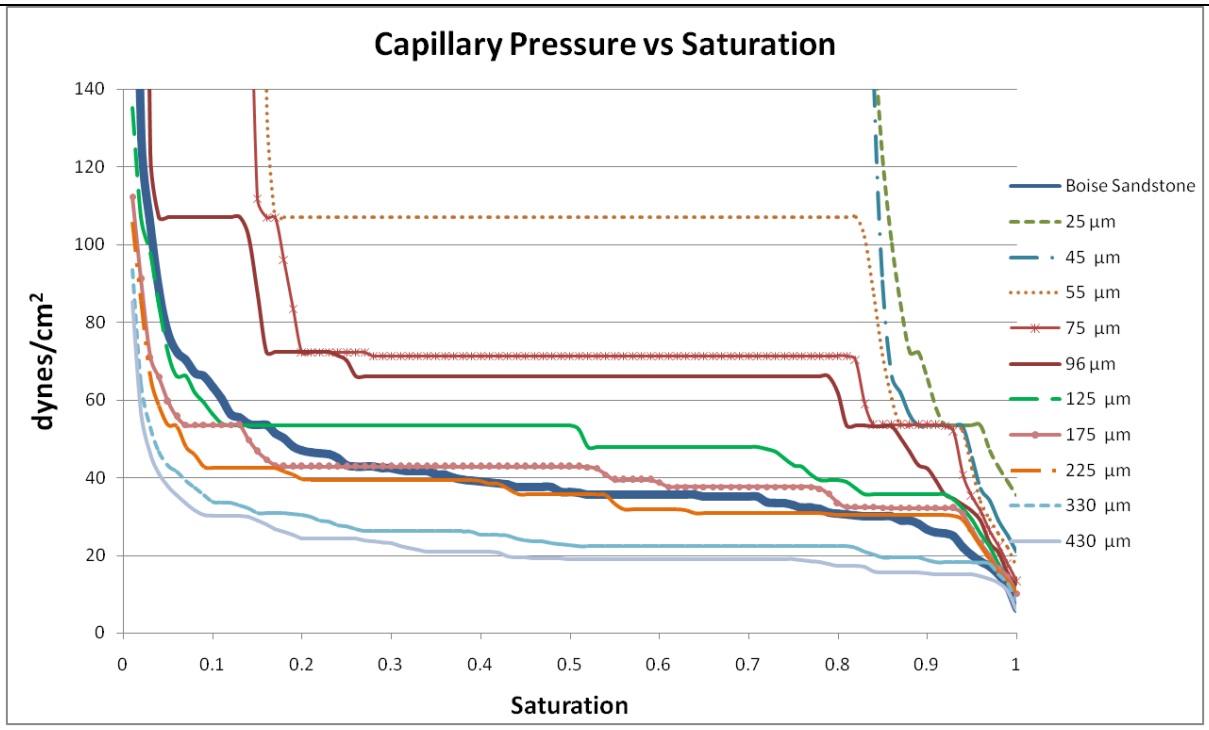

Figure 26. Capillary pressure curves for multiple micromodel depths as well as the original Boise sandstone, obtained by pore-network Quasi-static simulations.

As the depth increases, the capillary pressure required to saturate the pore space systematically

decreases. Figure 27, which shows the number of pores and throats for each depth average, gives a better understanding why. At low depths, increasing the depth average opens up connections between pores in the micromodel. Further increases add some new connections while simultaneously increasing the size of others already established. As the depth increases, the overall number of pores remains consistent at 400. Since the number of pores stays consistent, the decrease in the capillary pressure is due to the throats increasing in both number and radius. The number of throats increases until reaching 250 µm, where it begins to level off. At 250 µm, the slight decrease in the number of pores indicates that the network generation algorithm combines once separate pores to form larger pores. Since the number of throats remains level, it is likely that these pores retain most of the original throat connections.

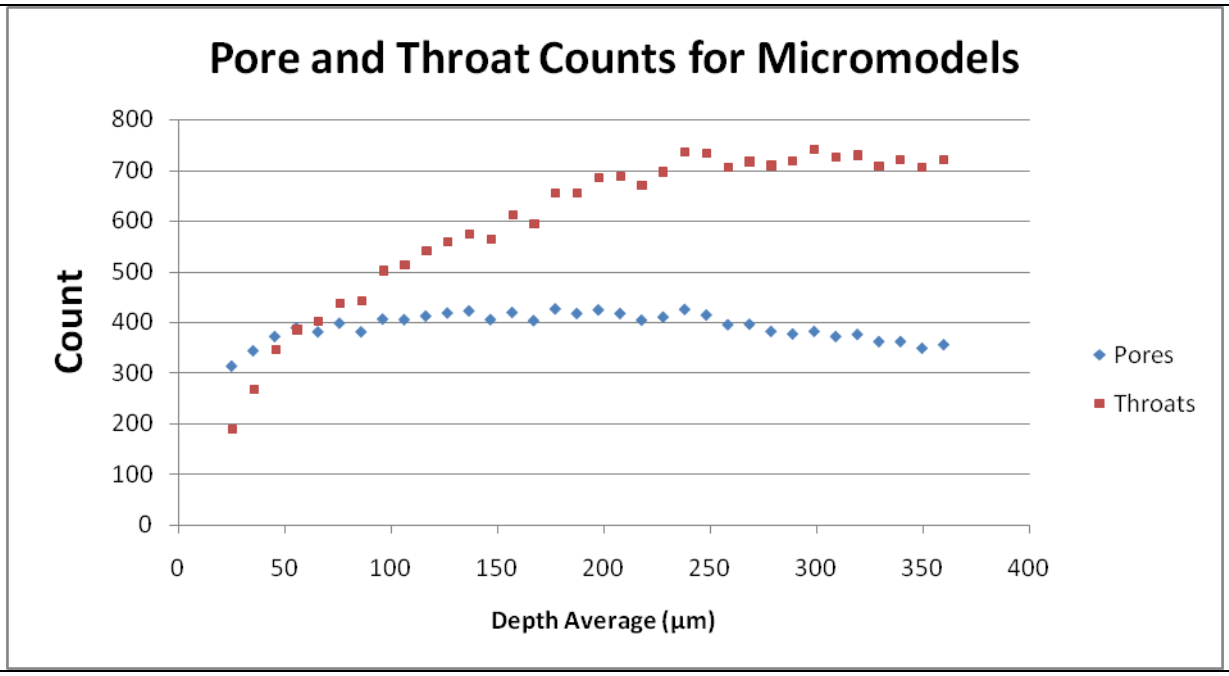

Figure 27. Pore and throat counts for micromodels of various depths.

4.4 Permeability Results

The error bars display a standard deviation for micromodels obtained from permeability calculations over a range of footprints for the depth average, which include areas of 1.03, 2.31, 4.11, and 6.42 mm^2. For a 400-$voxel^3$ (6.08 mm^3) cutout, a permeability of 2 Darcy was calculated. Simulations could not be performed for depth averages of below 7-voxels (25 μm) due to a lack of connectivity of the pore space. The best permeability match occurs at approximately 150 micron depth average.

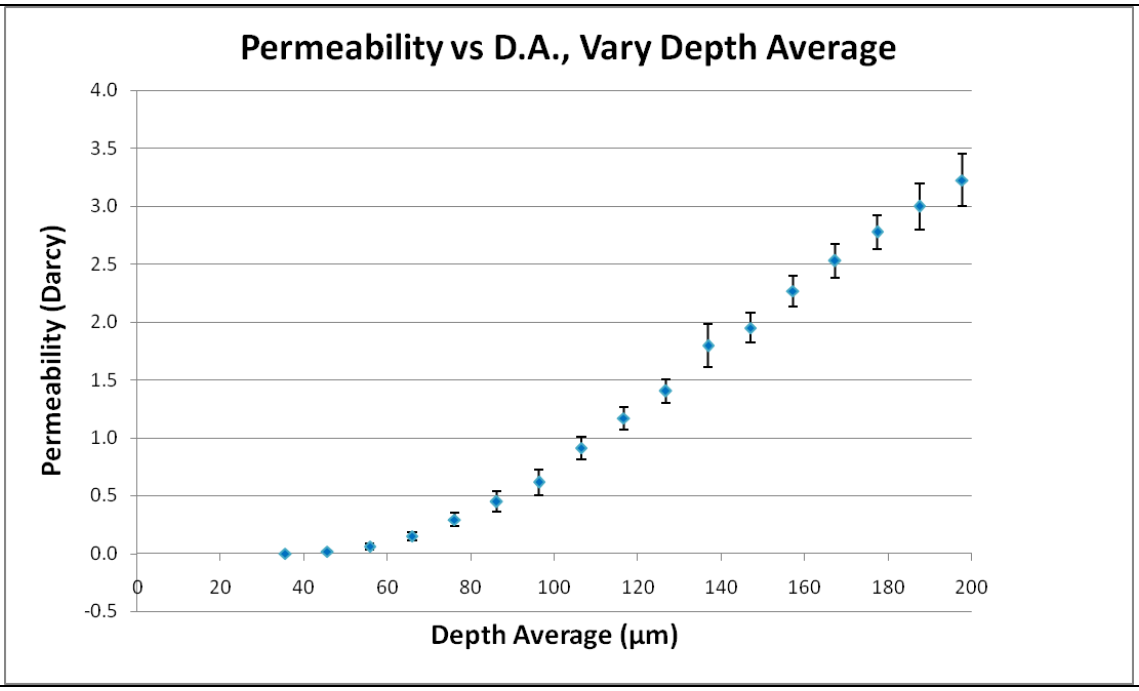

Figure 28. Permeabilities for micromodels up to 200 microns in depth.

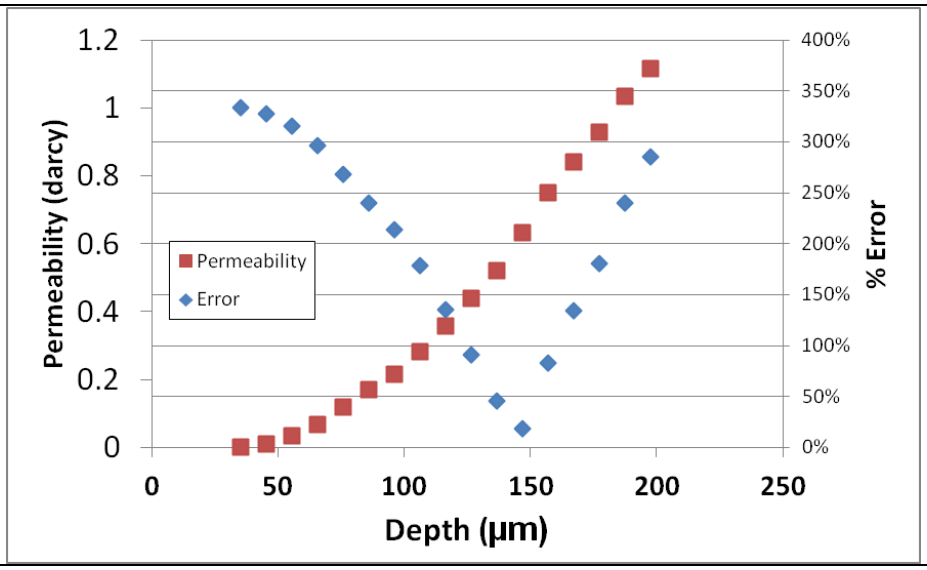

Figure 29. Permeability for each depth average (red), with a comparison to the original Boise sandstone, approximately 2 darcy for a 400-voxel^3 cutout.

4.5 Velocity Distribution Results

Although the permeability gives important insight, velocity distributions provide a more fundamental understanding of how well the micromodels reproduce flow behavior at a local level, while also allowing us to quantify whether they are able to induce flow in the third dimension. Since the pressure is kept constant across the direction of flow for all of the simulations, velocities are normalized with Darcy velocity in each simulation. This approach allows us to compare permeability (see previous section) independently of how well local flow patterns are reproduced.

Examining velocity distributions in the direction of flow (and their corresponding profiles displayed in Figure 30) confirm what is suggested by morphological parameters: for the 11-voxel (55 µm) depth average, the tortuosity and limited connectivity across the micromodel create a narrow velocity profile with a substantially lower (superficial?) velocity as compared to the

original Boise structure. Meanwhile, for large depths (200 μm), higher connectivity of the pore space than in the actual Boise sandstone corresponds to a longer tail in the distribution, indicating higher velocities in the direction of flow (39-voxel depth average). As can be seen in Figure 30, the velocity in the direction of flow is substantially higher (and more diffuse). This indicates more direct, less tortuous flow across the plane of the micromodel.

The distribution for the selected depth average, 23-voxels, shows good agreement in both in-plane velocity distributions (x in the direction of macroscopic flow and y orthogonal). For the vertical z-direction velocity profile, agreement with the true 3D structure is not as good. However, it does show that some velocity is generated in the third dimension, which is visualized in Figure 32, which displays the z-direction velocity profile. The regions that display 3-D flow are at throats, and diverging and converging channels.

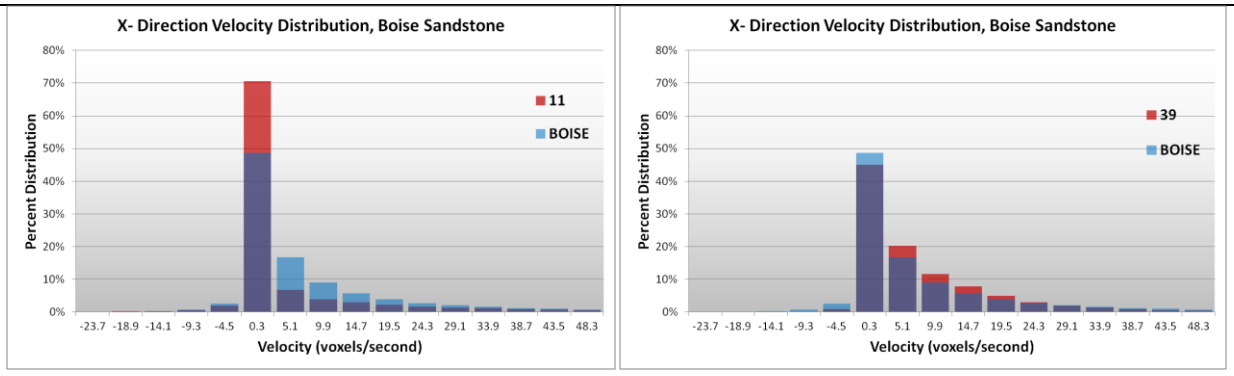

(a) (b)

Figure 30. Velocity distributions for (a) 11- and (b) 39-voxel depth averages compared to Boise sandstone.

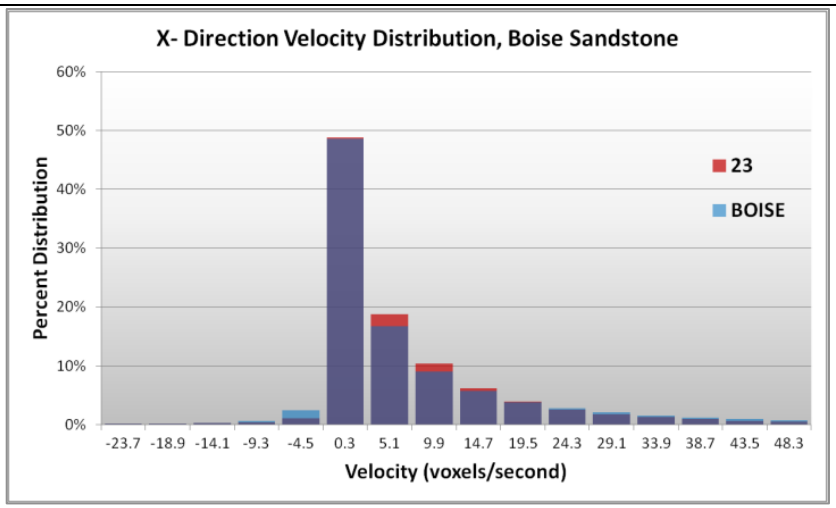

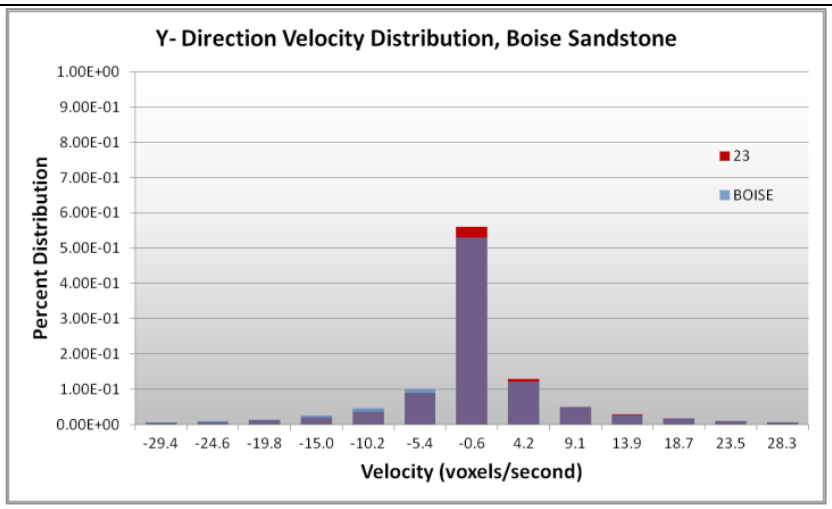

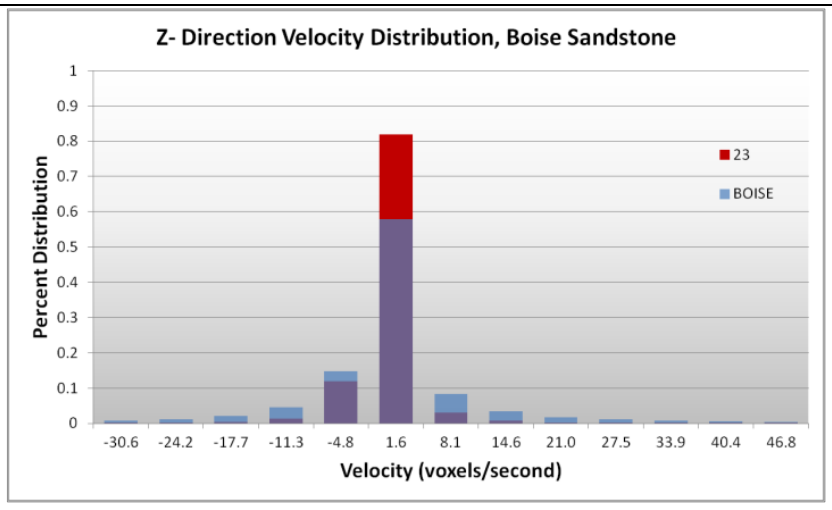

Figure 31.Velocity distributions for optimum depth (23-VDA).

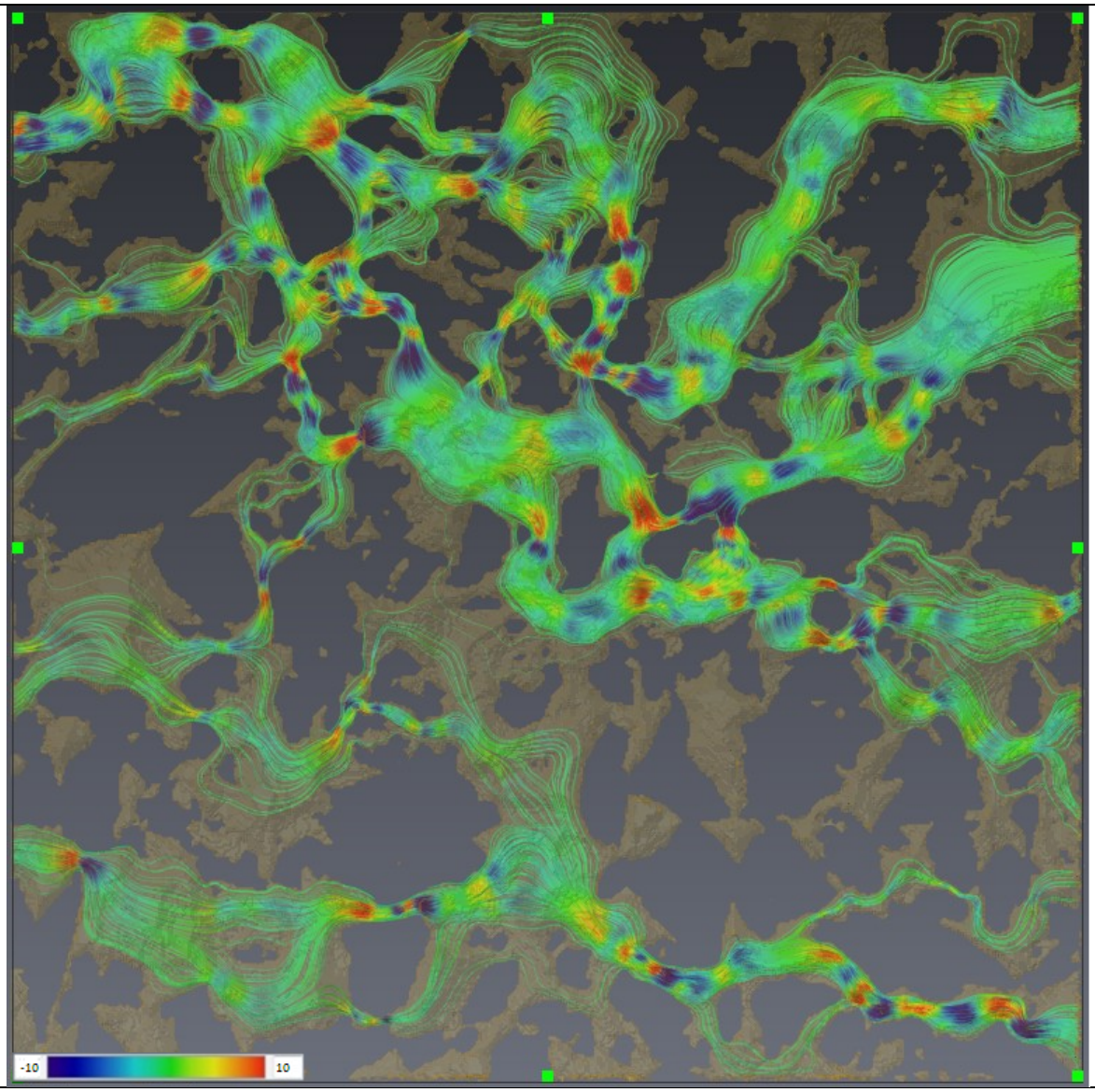

Figure 32. Velocity gradients for the z-direction (perpendicular to the page). Red indicates positive, blue negative.

4.6 Comparison of the 2.5-D micromodels to 2-D micromodels

2D micromodels were generated (from the same region as the 2.5-D micromodels) to compare the flow behavior to the 2.5-D micromodels. These 2D micromodels were created by taking a single slice from the 2.5-D micromodels and expanding them into 3D structures of equal height as the 2.5-D micromodels. The slices were taken from the 2.5-D micromodel designs ranging

Table 3. Sum of squares error for micromodels of different depths.

	VELOCITY DISTRIBUTION DATA		
Depth (μm)	SSE-X	SSE-Y	SSE-Z
25.35	1.0000	1.0000	1.0000
35.49	0.2794	0.3122	0.3694
45.63	0.1289	0.0923	0.1263
55.77	0.0619	0.0344	0.0990
65.91	0.0198	0.0133	0.0811
76.05	0.0132	0.0080	0.0762
86.19	0.0106	0.0070	0.0724
96.33	0.0073	0.0055	0.0693
106.47	0.0010	0.0024	0.0662
116.61	0.0009	0.0013	0.0635
126.75	0.0016	0.0016	0.0618
136.89	0.0046	0.0002	0.0359
147.03	0.0021	0.0012	0.0597
157.17	0.0022	0.0015	0.0587
167.31	0.0023	0.0017	0.0579
177.45	0.0029	0.0023	0.0568
187.59	0.0037	0.0027	0.0557
197.73	0.0042	0.0031	0.0542

from 23 to 29 voxels. Table 2 shows the results of velocity distribution sum of squares error analysis and permeabilities as compared to two 2.5-D optimum-depth designs. The 2.5-D models display more accurate velocity distributions in the direction of flow and transverse direction while also exhibiting velocity in the z-direction. A sum of squares error of .209 in the vertical direction indicates near-zero velocity for the 2D micromodel. One can also see that the 2-D micromodels that do display the least error in velocity are substantially more permeable than the actual Boise sandstone (2-darcy). This is believed to be a general observation with 2-D micromodels that are created by opening up channels for flow. Since the depth averaging process

does not change overall porosity in the region, it performs substantially better in terms of retaining realistic pore sizes while also preserving flow behavior.

Table 4. Velocity distributions, permeability, and porosity for depth averaged and 2D micromodels obtained from depth averaged slices.

DEPTH	VELOCITY DISTRIBUTION DATA			PERMEABILITY	POROSITY
Depth (Voxels)	SSE-X	SSE-Y	SSE-Z	darcy	Void Fraction
Boise				2.01	0.20
23-DA	0.0009	0.0013	0.0635	0.933	0.24
25-DA	0.0016	0.0016	0.0618	1.193	0.24
25-21	0.2711	0.2134	0.2098	0.56	0.45
25-22	0.1314	0.1364	0.2097	3.35	0.50
27-24	0.1147	0.1304	0.2096	4.25	0.52
23-21	0.0500	0.0694	0.2096	6.66	0.53
25-23	0.0297	0.0491	0.2097	8.73	0.56
27-25	0.0215	0.0378	0.2096	10.34	0.58
23-22	0.0092	0.0112	0.2096	14.15	0.58
29-27	0.0095	0.0139	0.2096	14.79	0.60
25-24	0.0080	0.0059	0.2095	16.80	0.61
27-26	0.0096	0.0039	0.2095	20.02	0.63
23-23	0.0131	0.0030	0.2094	20.44	0.62
29-28	0.0125	0.0033	0.2094	22.91	0.65
25-25	0.0181	0.0031	0.2096	23.50	0.65
27-27	0.0229	0.0040	0.2095	26.64	0.67
29-29	0.0328	0.0062	0.2095	30.45	0.69

4.7 Design of the Low Resolution Micromodel

Overview

The optimum design for the 2.5D micromodel at a resolution of 5 µm/pixel, based on all the parameters stated above with an emphasis on the velocity distributions, was set to 23 voxels in depth, or 117 µm. However, the available fabrication process and its limitations prevented us from etching at that scale. A minimum drill bit size of 25 µm and maximum aspect ratio of 2:1 at our LSU laboratory required lowering the resolution of the micromodel. We did this by

averaging 5x5x2 sections of the voxel images. The previous tests narrowed the region of interest to between 20 to 30 voxels (100-150 μm) depth average. We repeated FEM flow simulations.

Velocity distributions and the permeability were obtained for six depth averages between 100 and 150 μm. The results are displayed in Table 5. A depth of 26-voxels (13 different layers) was selected to fabricate (130 μm). A view of the depth averaged micromodel before and after lowering the resolution can be seen in Figure 34. The void space (displayed in the mesh) still retains most of the connectivity of the original 5.07 μm resolution. The two velocity profiles through micromodels in Figure 35 show that the low resolution micromodel is nearly identical to the original.

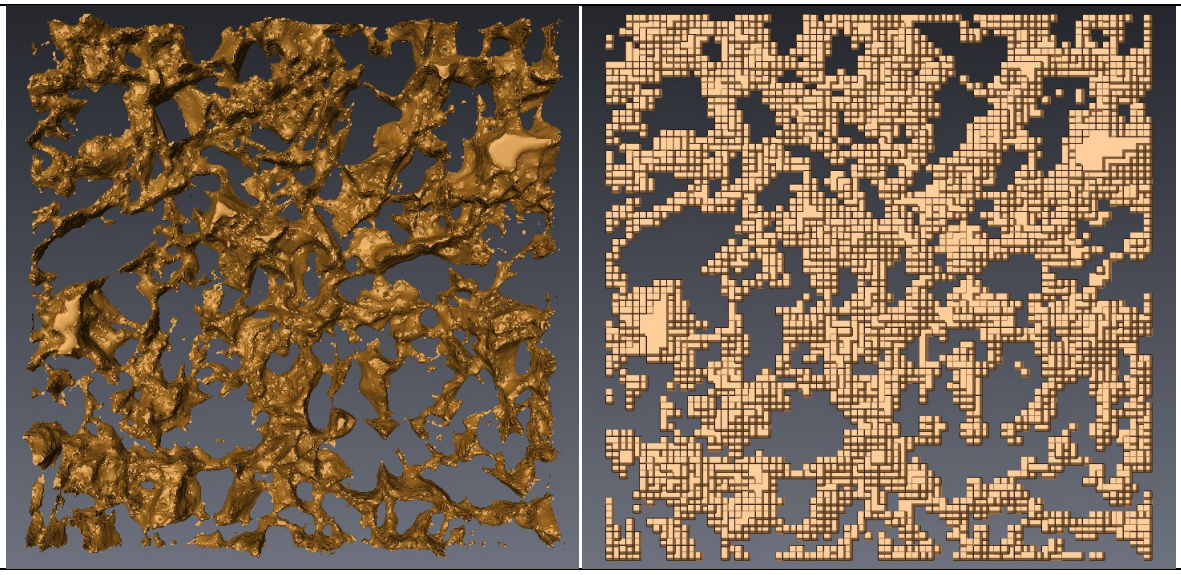

Figure 33. Image of 23-voxel micromodel before and after lowering the resolution.

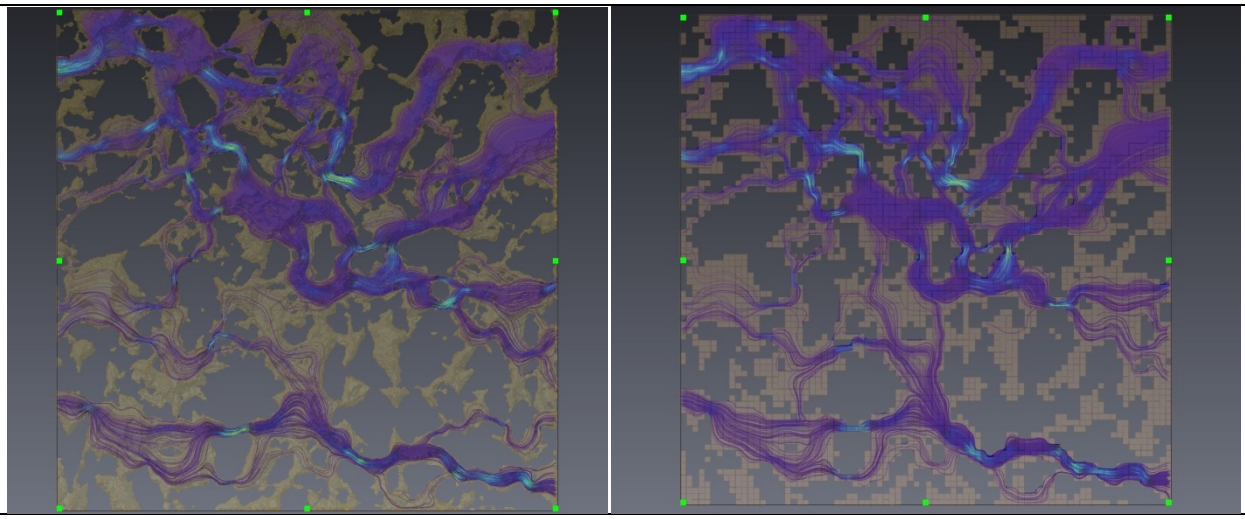

Figure 34. Image of the 23-voxel micromodels and their velocity distributions before and after lower the resolution.

Table 5. Flow-based results for the low-resolution micromodels.

LOW-RES		VELOCITY DISTRIBUTION DATA			PERMEABILITY
Depth (Voxels)	Depth (µm)	SSE-X	SSE-Y	SSE-Z	Fraction Error
20	101.4	0.0093	0.0087	0.0715	0.648
22	111.54	0.0021	0.0043	0.0681	0.573
24	121.68	0.0008	0.0035	0.0661	0.407
26	131.82	0.0008	0.0029	0.0642	0.282
28	141.96	0.0020	0.0021	0.0637	0.008
30	152.1	0.0015	0.0026	0.0616	0.085
Hi-Res Opt. (23)	116.61	0.0009	0.0013	0.0635	0.404

CHAPTER 5 SUMMARY

5.1 Conclusions

Using alternative microfabrication techniques, we have developed a new class of micromodels for which the floor height is varied, giving some variation in both flow and structure in the third dimension. In addition to allowing some flow in the third dimension, this approach enables us to created micromodel patterns directly from 3D x-ray microtomography data of real rocks. Simulations suggest that the new 2.5D rock-based micromodels are reasonably effective at retaining important morphologic and dynamic parameters from the real rock, including pore coordination number, permeability, and pore-scale velocity distributions.

We demonstrate the design technique using data from a Boise sandstone core sample imaged at 5.07 microns. The optimal micromodel pattern was created using a depth averaging over 116 μm of the original 3D data. This depth was selected based on a series of flow-based and morphological parameters that best matched the same characteristics of the original Boise sandstone image.

A review of the design process is displayed in Figure 31. Following X-ray microtomography of the core sample, a cut out of the image (a-b) is depth averaged and used to generate networks and finite element meshes (c) to obtain geometric, morphologic, and flow-based characteristics that help to identify the best depth average design. Flow-based testing is conducted once more using low-resolution micromodels (d) if necessary in a region bounded by the previous tests. The final micromodel design is then dividing into single slice images, where edge-detection software is then used to vectorize each cut out. These vectorized images are then sent to AutoCAD where the physical dimensions are labeled and final additions to the micromodel, such as the inlet and

exit reservoirs, are sent to the microfabrication group to produce the brass mold. Finally, a PMMA chip is generated for future studies (e).

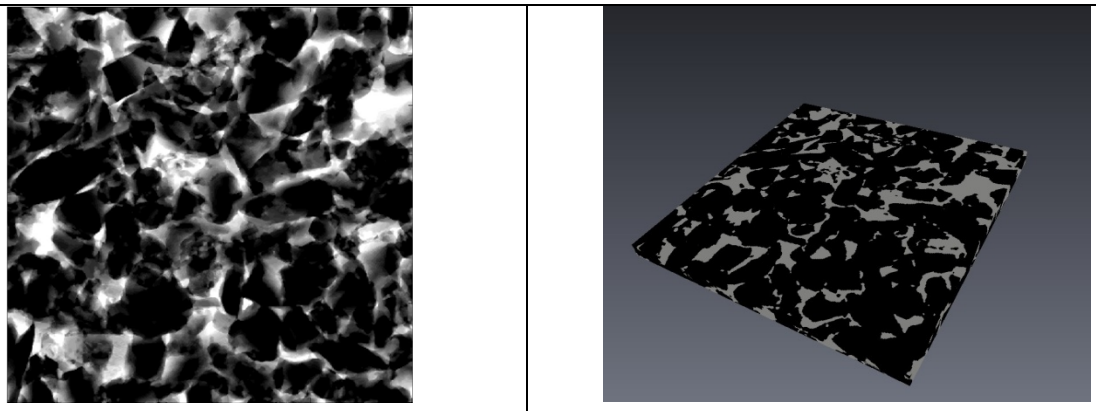

(a)

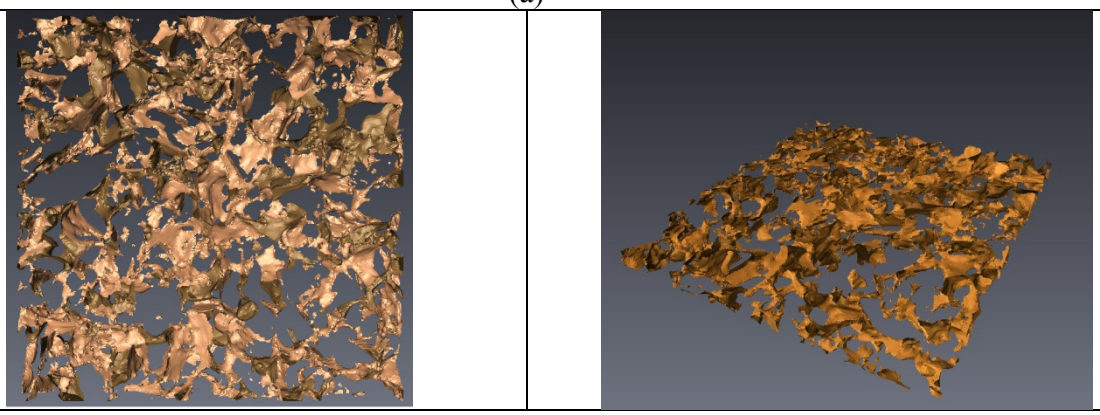

(b)

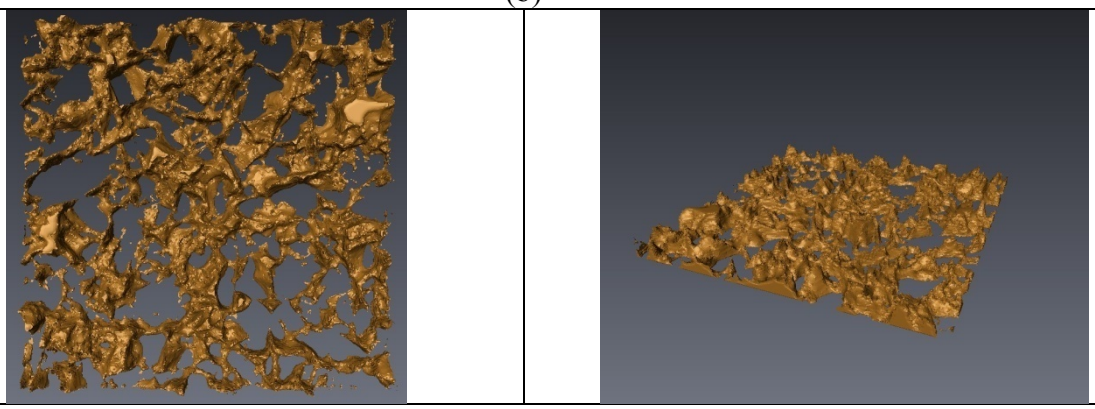

(c)

Figure 35 (a-c). Display of the 2.5-D depth averaging process through images: (a) the original cut-out Image, (b) the cut out translated to a 3D mesh, (c) the mesh following the depth averaging process, (d) the lower resolution mesh, (e) the final SEM image of the PMMA chip.

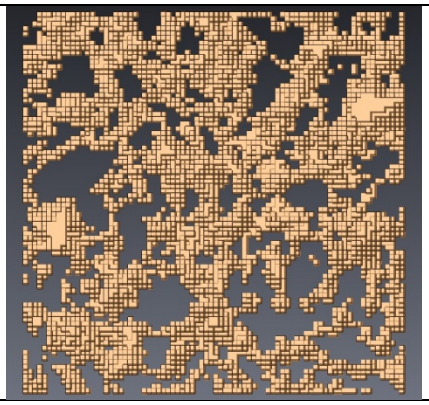

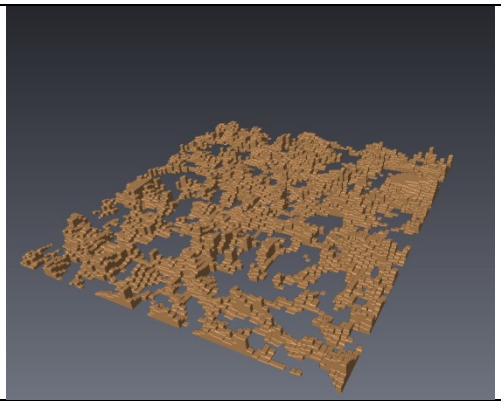

(d)

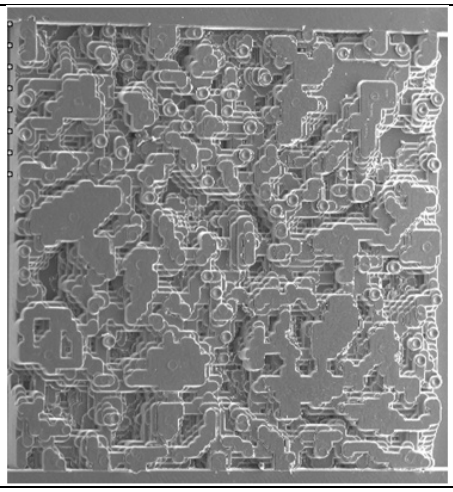

(e)

Figure 35 (d-e). Display of the 2.5-D depth averaging process through images: (a) the original cut-out Image, (b) the cut out translated to a 3D mesh, (c) the mesh following the depth averaging process, (d) the lower resolution mesh, (e) the final SEM image of the PMMA chip.

A number of techniques typically used to identify and characterize actual porous media were used as part of the optimization process to selecting the depth average that best replicated the characteristics of the original porous media sample. The relevant final parameters were the flow profile distributions, the permeability, the capillary pressure curves, the chord length distributions, and the pore-network morphological statistics. Two studied parameters, the two-point correlation function and the Minkowski functionals, were not usable.

A summary table containing all of the data is below. Because of the limitations of the equipment available to us, particularly a minimum drill bit radius of 25 µm, the resolution was reduced by 5x5x2 (25x25x10 μm^3) voxels into one unit. Using this reduced resolution, an optimum based on the velocity distributions and permeability gave us an ideal depth average of 26 voxels (131 µm). This design was then processed and handed to the microfabrication group at LSU to construct the brass mold insert. SEM images of the PMMA chips, developed by Daniel S. Park, are displayed in Figures 36, 37, and 38.

Table 6. Error Analysis Summary for High Resolution 2.5-D micromodel Boise sandstone designs.

DEPTH		VELOCITY DISTRIBUTION DATA			PERMEABILITY	CAPILLARY PRESSURE CURVE	CHORD LENGTH DISTRIBUTION	NETWORK STATISTICS- PORE DATA SSE				NETWORK STATISTICS- THROAT DATA SSE			
(Voxels)	(µm)	SSE-X	SSE-Y	SSE-Z	Fraction Error	SSE	SSE	Pore Coordination Number	Inscribed Pore Diameter	Inscribed Pore Volume	Inscribed Pore-Throat Diameter	Pore Throat Equivalent Diameter	Throat Aspect Ratio	Throat Lengths	Throat Conductivity
5	25.35	1.0000	1.0000	1.0000	1.000	212577355	0.147	0.061	0.1348	0.0006	0.0553	0.0356	0.0499	0.046	0.017
7	35.49	0.2794	0.3122	0.3694	1.000	178336208	0.064	0.022	0.0625	0.0003	0.0223	0.0069	0.0221	0.015	0.009
11	55.77	0.0619	0.0344	0.0990	0.946	4220275071	0.018	0.001	0.0359	0.0003	0.0063	0.0025	0.0184	0.009	0.004
15	76.05	0.0132	0.0080	0.0762	0.803	8131552	0.009	0.001	0.0273	0.0005	0.0028	0.0052	0.0258	0.007	0.002
19	96.33	0.0073	0.0055	0.0693	0.642	398659	0.005	0.005	0.0452	0.0022	0.0074	0.0137	0.0286	0.012	0.003
23	116.61	0.0009	0.0013	0.0635	0.404	21278	0.007	0.013	0.0453	0.0065	0.0106	0.0136	0.0267	0.015	0.003
27	136.89	0.0046	0.0002	0.0359	0.136	22255	0.008	0.017	0.0460	0.0064	0.0166	0.0210	0.0273	0.016	0.004
31	157.17	0.0022	0.0015	0.0587	0.247	20284	0.010	0.018	0.0545	0.0091	0.0117	0.0185	0.0326	0.015	0.004
35	177.45	0.0029	0.0023	0.0568	0.542	20647	0.017	0.022	0.0579	0.0102	0.0171	0.0224	0.0311	0.016	0.004
39	197.73	0.0042	0.0031	0.0542	0.855	22220	0.023	0.026	0.0634	0.0170	0.0218	0.0282	0.0302	0.022	0.005
43	218.01	N/A	N/A	N/A	1.000	24523	0.023	0.030	0.0629	0.0212	0.0150	0.0277	0.0365	0.017	0.005
47	238.29	N/A	N/A	N/A	1.000	27270	0.025	0.043	0.0693	0.0248	0.0272	0.0355	0.0366	0.026	0.009
51	258.57	N/A	N/A	N/A	1.000	32881	0.025	0.046	0.0775	0.0334	0.0269	0.0354	0.0372	0.022	0.007
55	278.85	N/A	N/A	N/A	1.000	38327	0.033	0.059	0.0866	0.0441	0.0336	0.0430	0.0410	0.028	0.010
59	299.13	N/A	N/A	N/A	1.000	42895	0.039	0.068	0.0993	0.0517	0.0457	0.0500	0.0373	0.034	0.012
63	319.41	N/A	N/A	N/A	1.000	48299	0.039	0.079	0.1009	0.0551	0.0479	0.0507	0.0367	0.034	0.013
67	339.69	N/A	N/A	N/A	1.000	52325	0.043	0.084	0.1159	0.0634	0.0502	0.0524	0.0384	0.037	0.016
71	359.97	N/A	N/A	N/A	#REF!	53295	0.041	0.079	0.1058	0.0726	0.0431	0.0450	0.0472	0.031	0.014

5.2 Future Works

The design of the micromodels is the first stage of the project for which the AEC is currently funding. These micromodels will be used in nanosensors flow experiments. Current micromodels (Figure 35) used in our experiments are designed by Crandall (2008). The 10 cm^2 micromodel is

a grid based design that has a pore width range of 200 μm-1000 μm and seven different depth levels ranging between 203 to 965 μm. This device has provided an extremely useful amount data (Park, 2011). The natural next step for the experiments is to determine how the nanosensors will act in an environment more like the actual reservoir. These experiments will provide us with a more realistic environment regarding the length scales and tortousity. We can then use these experimental results to develop a model that can predict with a high degree of accuracy the behavior of nanosensors through porous media.

An added benefit of developing a master mold is that we can provide variability to the micromodel without affecting the structure. For example, changing the wettability of the surface either locally or throughout the micromodel can provide an ample amount of information regarding how the nanosensors will react to local changes in the environment as well as across different reservoirs. One experiment currently being considered involves depositing clay at locations on the surface of the micromodel to determine how that will affect nanosensors behaviors. The ability to manipulate the micromodel's characteristics without affecting the structure will provide an array of opportunities to study the behavior of nanosensors through porous media.

A second micromodel is staged to be developed from a core sample being provided by the AEC. With the scripts in place, it should be possible to automate the optimization step. With the exception of the mesh generation, which is currently being done on a local computer with AVIZO, the codes are all on the HPC network or capable of being run on the network. If a different mesh generator is used, such as the one developed by Thompson, the process can be set

up to simply be given an input image and output an optimum design. This can be done by weighting the final sum of squares errors of each parameter to select an overall optimized depth.

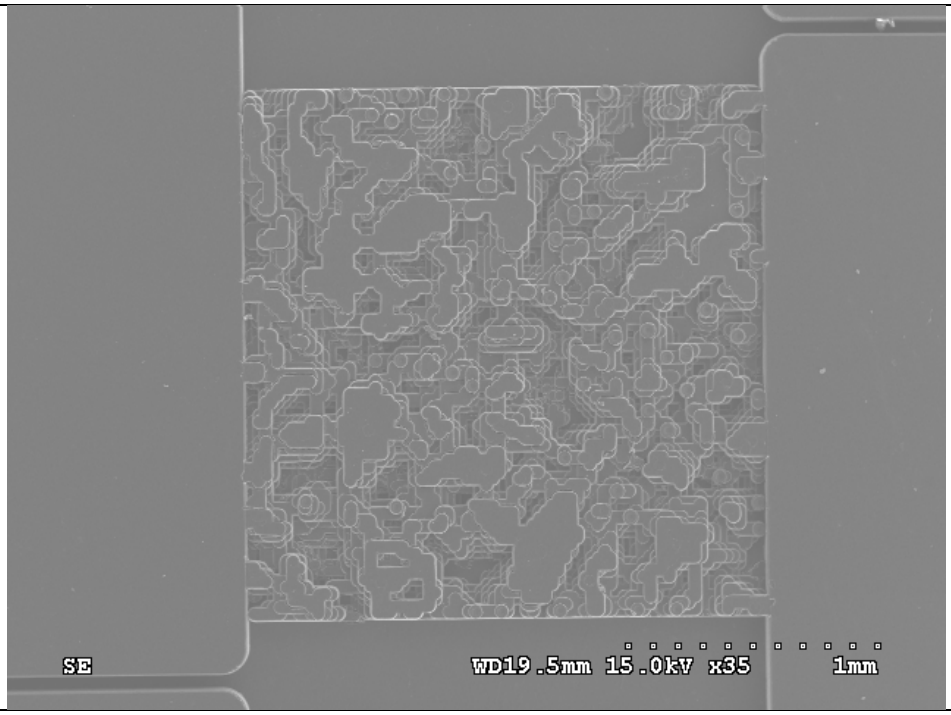

Figure 36. SEM image of fabricated micromodel.

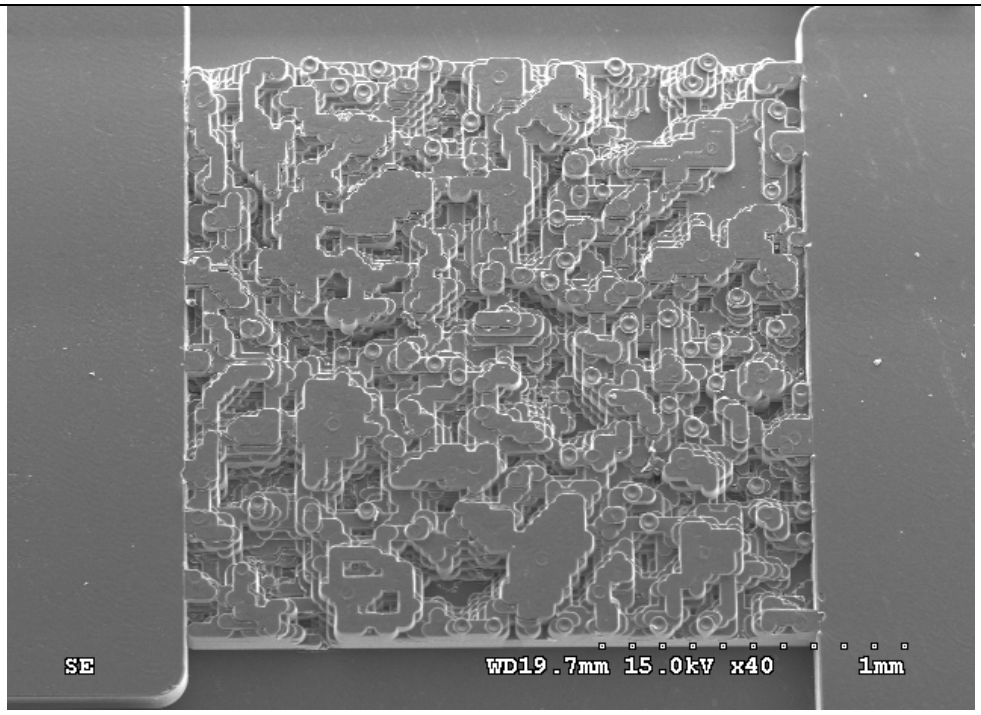

Figure 37. SEM image of fabricated micromodel.

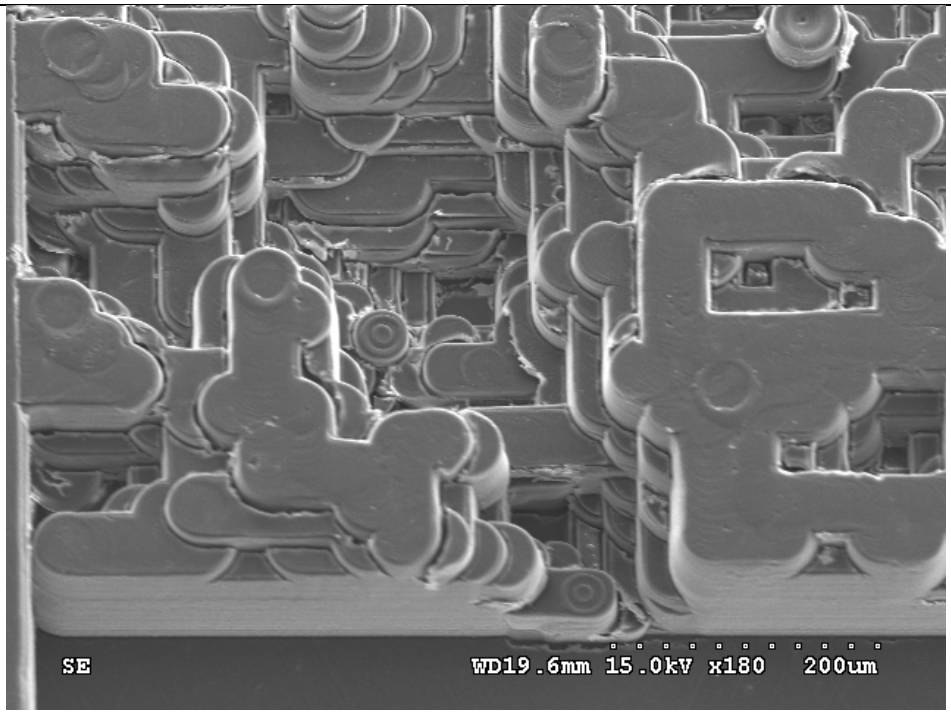

Figure 38. SEM image of fabricated micromodel, magnified.

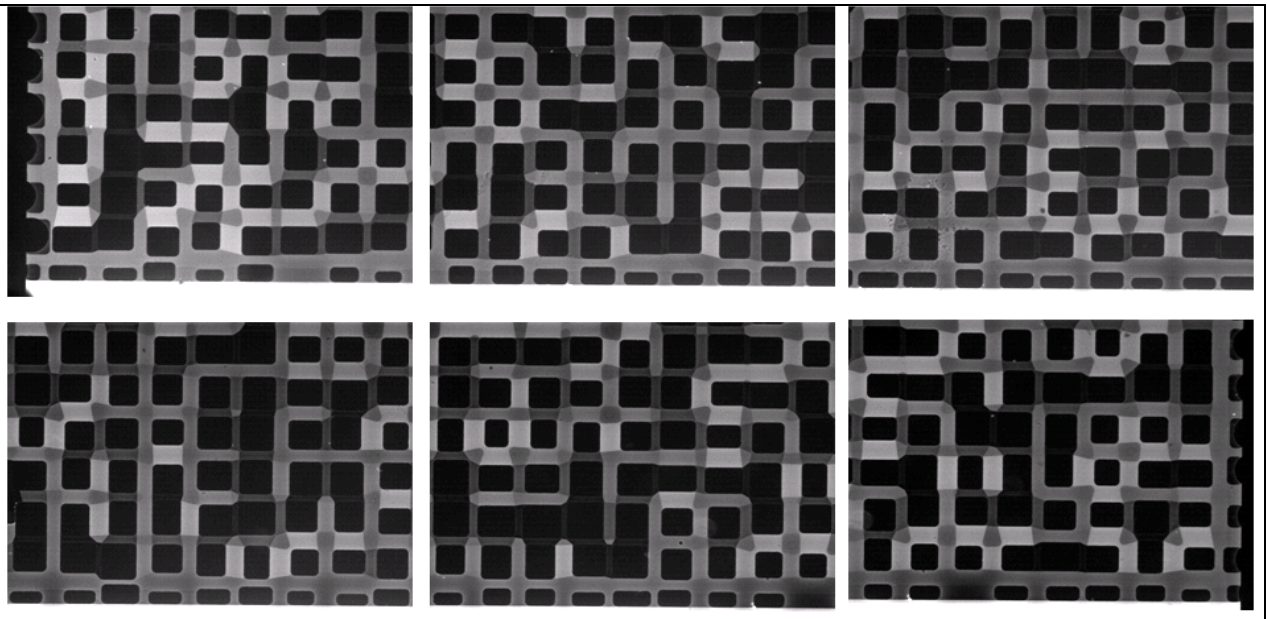

Figure 39. Close up images of the current micromodel design, developed from a design by Crandal (2008)

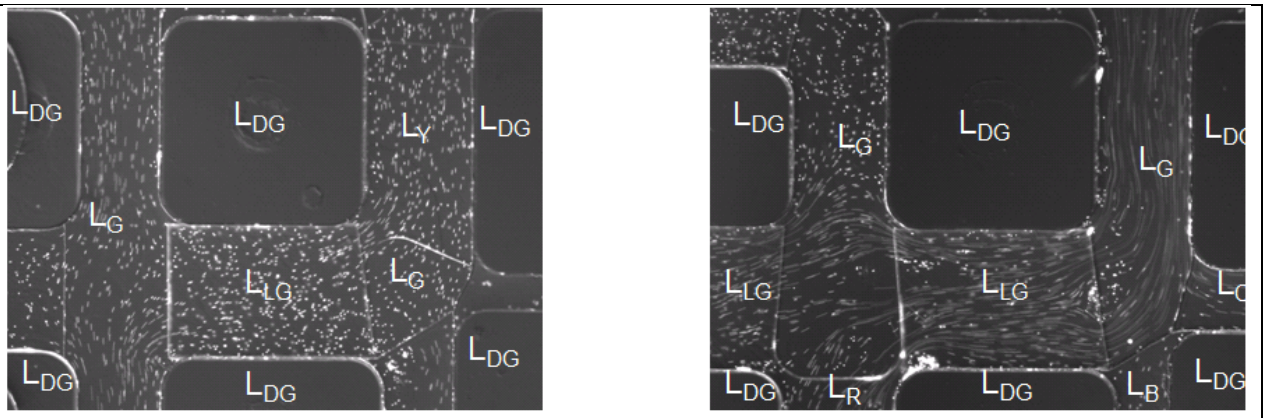

Figure 40. Close up images of the current micromodel design, developed from a design by Crandal (2008). Particles of 1micron size flow through the channels.

References

Al-Raoush, R., K., T., & Willson, C. (2003). Comparison of Network Generation Techniques for Unconsolidated Porous Media. *Soil Science Society of America* , 1687-1700.

Armitage, P., & Dawe, R. (1989). What is the Rheology of Foam in Porous Media? A Micromodel Study. *SPE International Symposium on Oilfield Chemistry* (pp. 323-334). Houston, TX: SPE.

Auset, M., & Keller, A. (2004). Pore-scale Processes that Control Dispersion of Colloids in Saturated Porous Media. *Water Resources Research* , 1-11.

Balhoff, M., & Thompson, K. (2006). A macroscopic model for shear-thinning flow in packed beds based on network modeling. *Chemical Engineering Science* , 698-719.

Berryman, J., & Blair, S. (1986). Use of digital image analysis to estimate fluid permeability of porous materials: Application of two-point correlation functions. *Journal of Applied Physics* , 1930 - 1938 .

Blasquez, I., & Pouraudeaux, J. (2003). Efficient processing of Minkowski functionals on a 3D binary image using binary decision diagrams. *Journal of WSCG* .

Boek. (2010). Fundamentals of fluid flow in porous media: Lattice-Boltzmann (LB) and beyond. Imperial College, London, England.

Boek, E., & Venturoli, M. (2010). Lattice-Boltzmann studies of fluid flow in porous media with realistic rock geometries. *Computers and Mathematics with Applications* , 2305-2314.

Browning, F. F. (1996). Fundamental study of the dissolution of calcium phosphonates from porous media. *AICHE Journal* , 2883-2896.

Bryant, S., & Mellor, D. (1993). Physically representative network models of transport in porous media. *AICHE Journal* , 387-396\.

Chang, S., Martin, F., & Grigg, R. (1994). Effect of Pressure on CO2 Foam Displacements: A Micromodel Visualization Study. *SPE/DOE Ninth Symposium on Improved Oil Recovery* (pp. 11-22). Tulsa, OK: SPE.

Chatzis, I., & Dullien, F. (1983). Dynamic Immiscible Displacement Mechanisms in Pore Doublets: Theory versus Experiment. *Journal of Colloid and Interface Science* , 199-222.

Coker, D., & Torquato, S. (1996). Morphology and physical properties of Fontainebleau sandstone via a tomographic analysis. *Journal of Geophysical Research* , 17,497-17,506.

Cottin, C., & Bodiguel, C. (2010). Drainage in two-dimensional porous media: From capillary fingering to viscous flow. *Physical Review E.* , 046315 1-10.

Crandall, e. (2008). A New Stereolithography Experimental Porous Flow Device. *Review of Scientific Instruments* .

Debye, P. e. (1957). Scattering by an Inhomogeneous Solid. II. The Correlation Function and Its Application . *Journal of Applied Physics* , 679 - 683.

George, D., Hayat, O., & Kovscek, A. (2005). A Microvisual Study of Solution-Gas-Drive Mechanisms in Viscous Oils. *Journal of Petroleum Science and Engineering* , 101-119.

Gunda, N., & et.al. (2011). Reservoir-on-a-Chip (ROC): A new paradigm in reservoir engineering. *Lab On A Chip* , 3785-3782.

Hazlett, R. (1997). Statistical Characterization and Stochastic Modeling of Pore Networks in Relation to Fluid Flow. *Mathematical Geology* , 802-822.

Hidijat, I. e. (2002). Transport Properties of Porous Media Reconstructed From Thin-Sections . *SPE Journal* , 40-48.

Hilfer, R. (1991). Geometric and Dielectric Characterization on Porous Media. *Physical Review B* , 62-75.

Hornbrook, J., Casatnier, L., & Pettit, P. (1991). Observation of Foam-Oil Interactions in a New, High Resolution Micromodel. *66th Annual Technical Conference and Exhibition of the Society of Petroleum Engineers* (pp. 377-382). Dallas, TX: SPE.

Hornof, V., & Morrow, N. (1998). Flow Visualization of the Effects of Interfacial Tension on Displacement. *SPE Reservoir Engineering* , 251-256.

Ioannidis, M., & Chatzis, I. (2000). On the Geometry and Topology of 3D Stochastic Porous Media. *Journal of Colloid and Interface Science* , 323-334.

Jamaloei, B., & Kharrat, R. (2010). Analysis of Microscopic Displacement Mechanisms of Dilute Surfactant Flooding in Oil-Wet and Water Wet-Porous Media. *Transportation in Porous Media* , 1-19.

Javadpour, F., & Fischer, D. (2008). Nanotechnology-Based Micromodels And New Image Analysis to Study Transport in Porous Media. *Journal of Canadian Petroleum Technology* , 30-37.

Lake, L. (1989). *Enhanced Oil Recovery.* Upper Saddle River, NJ: Prentice Hall.

Lehmann, P. e. (2008). Tomographical Imaging and Mathematical Description of Porous Media Used for the Prediction of Fluid Distribution. *Vadose Zone Journal* , 5:80-97.

Lindquist, W., & Venkatarangan, A. (1999). Investigating 3D Geometry of Porous Media from High Resolution Images. *Phys. Chem. Earth* , 593-599.

McDowell, A. *X-ray Tomography.* Lawrence Berkeley National Laboratory, Berkeley, CA.

McDowell, A. (2007). *X-ray Tomography.* Lawrence Berkeley National Laboratory, Berkeley, CA.

McKellar, M., & Wardlaw, N. (1982). A Method of Making Two-dimensional Glass Micromodels of Pore Systems. *Journal of Canadian Petroleum Technology* , 39-41.

Mecke, K. (2000). Additivity, Convexity, and Beyond: Applications of Minkowski Functionals in Statistical Physics. *LNP 554* , 111-184.

Mecke, K., & Arns, C. (2005). Fluids in Porous Media: a Morphometric Approach. *Journal of Physics: Condensed Matter* , S503-S534.

Michielsen, K., & De Raedt, H. (2002). Aspects of Mathematical Morphology. *Advances in Imaging and Electron Physics* , 1-30.

Michielsen, K., & De Raedt, H. (2000). Morphological Characterization of Spatial Patterns. *Progress of Theoretical Physics Supplement* , 543-548.

Mohiuddin, Z., & M., H. (2011). Visualization of CO2 Displacement Under Gravity Domination. *SPE Enhanced Oil Recovery Conference*, (pp. 1-13). Kuala Lumpur, Malaysia.

Morrow, N. (1990). Wettability and Its Effect on Oil Recovery. *Journal of Petroleum Technology* , 1476-1484.

Muecke, T. (1979). Formation Fines and Factors Controlling their Movement in Porous Media. *Journal of Petroleum Technology* , 144-150.

Øren, P. E., Bakke, S., & Arntzen, O. (1998). Extending Predictive Capabilities to Network Models. *SPE Journal* , 324-336.

Owete, O., & Brigham, W. (1987). Flow Behavior of Foam: A Porous Micromodel Study. *SPE Reservoir Engineering* , 315-323.

Park, D. S. (2011). Flow Visualization in Artificial Porous Media from Microfluidic PMMA Devices. *ASME International Mechanical Engineering Congress & Expo* (pp. IMECE2011-65266). Denver, CO: ASME.

Paterson, L., Hornof, V., & Neale, G. (1984). Visualization of a Surfactant Flood of an Oil-Saturated Porous Medium. *Society of Petroleum Engineers Journal* , 325-327.

Pourafshary, P., & et.al. (2009). Priority Assessment of Investment in Development of Nanotechnology in Upstream Petroleum Industry. *SPE Saudi Arabia Section Technical Symposium, 9-11 May 2009* (pp. 1-11). AlKhobar, Saudi Arabia: SPE.

Roberts, A., & Knackstedt, M. (1996). Structure-Property Correlations in Model Composite Materials. *PHYSICAL REVIEW E* , 2313 - 2328.

Sayegh, S., & Fisher, D. (2008). Enhanced Oil Recovery by CO2 Flooding in Homogeneous and Heterogeneous 2D Micromodels. *Canadian International Petroleum Conference/SPE Gas Technology Symposium 2008 Joint Conference* (pp. 1-16). Calgary, Alberta, Canada: Petroleum Society.

Sohrabi, M., Danesh, A., & Jamiolahmady, M. (2007). Visualisation of Residual Oil Recovery by Near-miscible Gas and SWAG Injection Using High-pressure Micromodels. *Transportation in Porous Media* , 239-257.

Sok, R., & Knackstedt, M. (2002). Direct and Stochastic Generation of Network Models from Tomographic Images; Effect of Topology on Residual Saturations. *Transport in Porous Media* , 345–372.

Thompson, K., & Fogler, H. (1997). Modeling Flow in Disordered Packed Beds from Pore-Scale Fluid Mechanics. *Fluid Mechanics and Transport Phenomena* , 1377-1389.

Torquato, S., & Lu, B. (1993). Chord-length distribution for two-phase random media. *Physical Review E.*, 2950-2953.

Tsakiroglou, C. D., & Avraam, D. G. (2002). Fabrication of a new class of porous media models for visualization studies of multiphase flow processes. *Journal of Material Science* , 353-363.

TSAKIROGLOU, C. D., & AVRAAM, D. G. (2002). Fabrication of a new class of porous media models for visualization studies of multiphase flow processes. *Journal of Material Science* , 353-363.

van Dalen, G. e. (2003). 3-D Imaging of Foods Using X-Ray Microtomography. *G.I.T. Imaging and Technology* , 18-21.

Vogel, H. (2002). Topological Characterization of Porous Media. *LNP 600* , 75-92.

Wardlaw, N. (1980). The Effects of Pore Structure on Displacement Efficiency in Reservoir Rocks and in Glass Micromodels. *SPE/DOE Enhanced Oil Recovery Symposium* (pp. 345-352). Tulsa, OK: SPE.

Willingham, T., Werth, C., & Valocchi, A. (2008). Evaluation of the Effects of Media Structure on Mixing-Controlled Reactions Using Pore-Scale Modeling and Micromodel Experiments. *Environmental Science and Technology* , 3185-3193.

Zhang, C., & et.al. (2011). Liquid CO2 Displacement of Water in a Dual-Permeability Pore Network Micromodel. *Environmental Science and Technology* , 7581-7588.

VITA

Saade Bou-Mikael was born May 27, 1986, in Metairie, Louisiana. In 1997 he moved, along with his family, to Sumatra, Indonesia, for his father's overseas assignment for Caltex, where he lived for three years before coming back to New Orleans to attend Jesuit High School. Following his graduation in 2004, he elected to study biomedical engineering at Tulane; however, a small weather catastrophe known as Katrina brought him to LSU as a temporary student in 2005, where he fell in love with the university. He transferred to the Cain Department of Chemical Engineering in 2006, and received his Bachelor's Degree in 2009. Following his graduation, he declined an opportunity to attend graduate school at Penn State to remain at LSU researching under Dr. Karsten Thompson.